ICFA

SLAC-J-ICFA-21
Fall 2000
SLAC-R-652

HOME PAGE

http://www.slac.stanford.edu/pubs/icfa/

ICFA INSTRUMENTATION BULLETIN*

The publication of the ICFA Instrumentation Bulletin is an activity of the Panel on Future Innovation and Development of ICFA (International Committee for Future Accelerators).

Volume 21

• Fall 2000 Issue

---

* Supported by the Department of Energy, contract DE-AC03-76SF005 15.

ICFA INSTRUMENTATION BULLETIN

The publication of the ICFA Instrumentation Bulletin is an activity of the Panel on Future Innovation and Development of ICFA (International Committee for Future Accelerators). The Bulletin reports on research and progress in the field of instrumentation with emphasis on application in the field of high-energy physics. It encourages issues of generic instrumentation.

Publisher : Stanford Linear Accelerator Center
SLAC Publications Department
Stanford, CA 94309, U.S.A.

Editor : J. Va'vra

Web Technical Advisers : J. Schwiening

The views expressed in this Bulletin do not necessarily represent those of the ICFA Panel or the editor. In all cases, the authors are responsible for their manuscripts. The printed version is mailed out in limited numbers to institutions on the SLAC Instrumentation mailing list. Issues of the ICFA Instrumentation Bulletin are accessible electronically on our Web site:

http://www.slac.stanford.edu/pubs/icfa/

Cover: The illustration depicts L. J. Waghenaer's marine atlas, "The Mariner's Mirror," published in 1588. Lucas Janszoon Waehenaer was born in Holland in the 1530s. He became a famous ship pilot in his time. In 1584, he published the atlas ("Spieghel der Zeevaerdt") which was greatly valued among mariners for centuries. This was not due only to the map content, but also to the detailed knowledge of navigation techniques of that time. The atlas, as it appears on our page, is the same one used for the Dutch to English translation.

Conference List

- ICFA School on Instrumentation in Particle Physics, Near Cape Town, South Africa, March 26 to April 6,2001 (http://www.nac.ac.za/icfa2001).

- IEEE Nuclear Science Symposium (NSS) And Medical Imaging Conference (MIC), 4-10 Nov 2001, San Diego, California (http://www.nss-mic.org/NSS.htm).

Table of Contents

Thin Calorimetry for Cosmic-Ray Studies Outside the Earth's Atmosphere

Richard WIGMANS

Department of Physics, Texas Tech University, Lubbock TX 79409-1051, USA

(wigmans@ttu.edu)

Abstract

Cosmic ray experiments outside the Earth's atmosphere are subject to severe restrictions on the mass of the instruments. Therefore, it is important that the experimental information that can be obtained per unit detector mass is maximized. In this paper, tests are described of a thin (1.4 $\lambda_{\rm int}$ deep) hadron calorimeter that was designed with this goal in mind. This detector was equipped with two independent active media, which provided complementary information on the showering hadrons. It is shown that by combining the information from these media it was possible to reduce the effects of the dominant leakage fluctuations on the calorimeter performance.

1 Introduction

In recent years, there has been an increased interest in the use of calorimetric techniques in cosmic-ray experiments outside the Earth's atmosphere. Calorimeters have been applied in experiments carried out in stratospheric balloon flights, in satellites and in the Space Shuttle. Several experiments are currently being planned for the International Space Station. These experiments focus on measuring features of the cosmic rays that are inaccessible with Earth-bound detectors, *e.g.,* the antiproton content, the chemical and isotopic composition and the high-energy electron and photon spectra.

One common aspect of all these experiments is the severe restriction on the mass of the detectors. For calorimeters, this restriction poses a new challenge: *How can one maximize the calorimetric information per unit detector mass?*

When high-energy hadrons develop showers in a 1–2 $\lambda_{\rm int}$ deep calorimeter, the response function is completely determined by leakage fluctuations. These fluctuations are very likely correlated with the fraction of energy spent on π^0 production inside the detector. In general, π^0s produced in the first nuclear interaction develop electromagnetic (em) showers that are contained in the detector, while charged pions typically escape. Therefore, events in which a large fraction of the initial energy is converted into π^0s in the first interaction will exhibit little leakage (a large detector signal), while events in which a small fraction of the energy has been transferred to π^0s will be characterized by large leakage (small detector signals).

It has been demonstrated experimentally that calorimeters using quartz fibers as active material are almost exclusively sensitive to the π^0 component of hadron showers [1]. This is because most of the energy in the non-em component is deposited by non-relativistic shower particles, which do not emit Čerenkov light, the source of experimental information in this type of detector [2].

We have used this feature in an attempt to get a handle on the (leakage) fluctuations that dominate the performance of very thin hadron calorimeters, and thus improve this performance. A dual-readout calorimeter that measures both the ionization losses (dE/dx) and the production of Čerenkov light might distinguish between events with relatively small and large shower leakage, since the ratio of the two signals would be different in these two cases: A relatively large Čerenkov signal would indicate relatively little shower leakage, while a small Čerenkov signal (compared to the dE/dx signal) would suggest that a large fraction of the shower energy escaped from the detector.

A group at TTU has built and tested such a calorimeter, in the framework of prototype studies for the Advanced Cosmic Composition Experiment at the Space Station (ACCESS). In this paper, some results of beam tests of this calorimeter are presented.

2 The detector

The calorimeter consisted of 39 lead plates (with a thickness of 6.4 mm each, for a total depth of 1.4 $\lambda_{\rm int}$ or 46 X_0). These plates were interleaved with alternating ribbons of scintillating and quartz fibers, providing x, y-readout and an effective tower structure for particles entering perpendicular to the absorber plates, for both types of light (Figure 1).

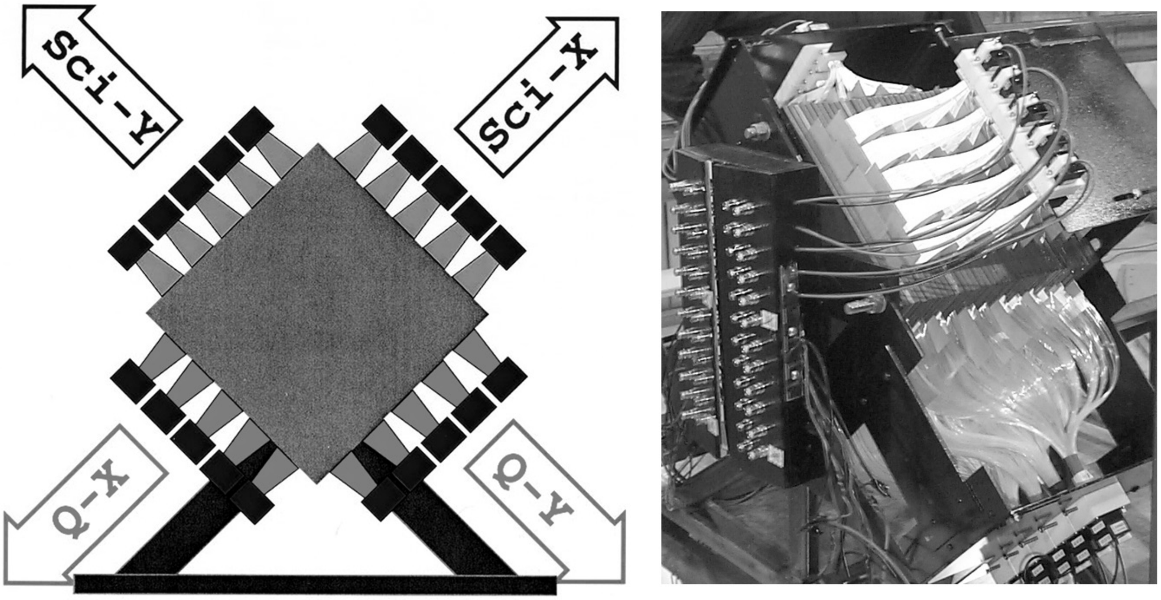

Figure 1: Schematic layout of the dual-readout calorimeter (left) and a photograph showing part of the actual instrument (right). See text for details.

The scintillating fibers[1] were 500 μm thick and had a numerical aperture of 0.72. The quartz fibers[2] were 270 μm thick and their numerical aperture was 0.40. The showering particles generated scintillation light in the plastic fibers and Čerenkov light in the quartz fibers. Photons emitted within the numerical aperture of the fibers were captured and transported through internal reflection to the fiber ends, where they were converted into photoelectrons in the photocathode of a photomultiplier tube (PMT)[3].

The fiber ribbons were inserted between the absorber plates according to the following scheme. Plate 1 was followed by a layer of quartz fibers oriented in the x direction (Q_x), plate 2 by a layer of quartz fibers oriented in the y direction (Q_y). The first layer of scintillating fibers (S_x, oriented in the x direction) was located behind absorber plate 3. Plates 4,5 and 6 were followed by layers of the types Q_x, Q_y and S_y, respectively. This pattern for the first six sampling layers was repeated subsequently.

Each fiber layer consisted of five 40 mm wide ribbons. The instrumented detector volume thus comprised a surface area of 20×20 cm^2 that extended over a depth of 28 cm. The five ribbons were read out separately, combined with the corresponding ribbons located at other depths in the structure. For example, the Q_x ribbons located behind absorber layers #1,4,7,10,13,16,19,22,25,28,31,34 and 37 were ganged together in five bunches read out by five PMTs. Also the S_x, S_y and Q_y ribbons were read out by five PMTs each, giving a total of 20 electronic channels.

---

[1] SCSN-81, a polystyrene-based product manufactured by Kuraray Inc., Japan

[2] Manufactured by Fiberguide Industries, USA

[3] Hamamatsu R5900U, 10-stage

Because of the way the signals were read out, the calorimeter had a tower structure for particles entering it perpendicular to its front surface. In total, there were 25 towers, each with a cross section of 4×4 cm^2, both for the scintillating-fiber and the quartz-fiber signal readout.

This detector was tested in the H2 beam line of the SPS at CERN. It was mounted on a platform that could be moved vertically and laterally, so that the center of each tower could be moved into the beam, as needed for calibration purposes. Usually, the angle (θ) between the beam and the calorimeter's front face was $0°$. However, we also performed some measurements in which the detector was rotated, at angles up to $\theta = 90°$.

Upstream of the calorimeter, a trigger counter telescope was installed, which allowed a choice of the beam spot size for the recorded events. Downstream of the calorimeter, a large scintillation counter served as the "tail catcher". The hadron measurements were carried out with a $0.25\lambda_{\rm int}$ carbon target installed directly in front of the calorimeter. Scintillation counters placed directly upstream and downstream of this target made it possible to select events in which the beam particle had interacted in it. In the electron measurements, this target was replaced by a Preshower Detector, consisting of a 5 mm thick lead plate, followed by a scintillation counter. This device was very useful for eliminating hadron and muon contamination at very high energies.

All individual calorimeter cells were calibrated with 150 GeV electrons incident on the cell center.

3 Test results

3.1 *Electron measurements*

The detector was exposed to beams of electrons with energies of 50, 100, 150, 200, 250 and 300 GeV. The signal distributions of both the scintillating fibers and the quartz fibers were well described by Gaussian functions. The energy resolutions were measured to scale with $E^{1/2}$: $\sigma/E = 50\%/\sqrt{E}$ for the scintillating fibers, and $140\%/\sqrt{E}$ for the quartz fibers.

As was also found in tests of other quartz fiber calorimeters, the em resolution of the quartz component of our detector was completely dominated and determined by *photoelectron statistics* [1]. On average, em showers produced 0.5 photoelectrons per GeV deposited energy in the quartz fibers. For 200 GeV em showers, the signal was thus, on average, composed of 100 photoelectrons. Statistical fluctuations in that number led to an energy resolution of 10%. The em energy resolution measured with the scintillating fibers was dominated by *sampling fluctuations*, with a minor contribution from photoelectron statistics (the light yield was 20 p.e./GeV in this case).

The electron measurements also illustrated clearly the differences between the angular distributions of the scintillation light and the Čerenkov light produced by the shower particles (see Figure 2). The scintillation light is emitted isotropically when excited molecules in the scintillating fibers return to their ground state. On the other hand, the Čerenkov light is emitted in a cone with a 46° opening angle centered around the direction of the relativistic shower particles. As the angle of the incident electron beam was changed, the ratio of the signals observed in the x and y scintillating fibers was found to be essentially constant, whereas the ratio of the signals from the x and y quartz fibers strongly depended on the direction of the incoming particles. The latter effect was quantitatively in good agreement with the angular dependence of the signals from em showers measured in other quartz fiber calorimeters [3, 4].

The observed effect offers the opportunity to use the dual-readout calorimeter as a *goniometer*. A comparison of the total signals from the two perpendicular sets of quartz fibers provides information about the angle of incidence of the showering particles, a nice and unforeseen bonus.

3.2 *Hadron measurements*

Mainly as a result of the effects of incomplete shower containment, the signal distributions for high energy hadrons from this thin detector looked very different from the electron ones. Figure 3 shows some results for 375 GeV π^-. In

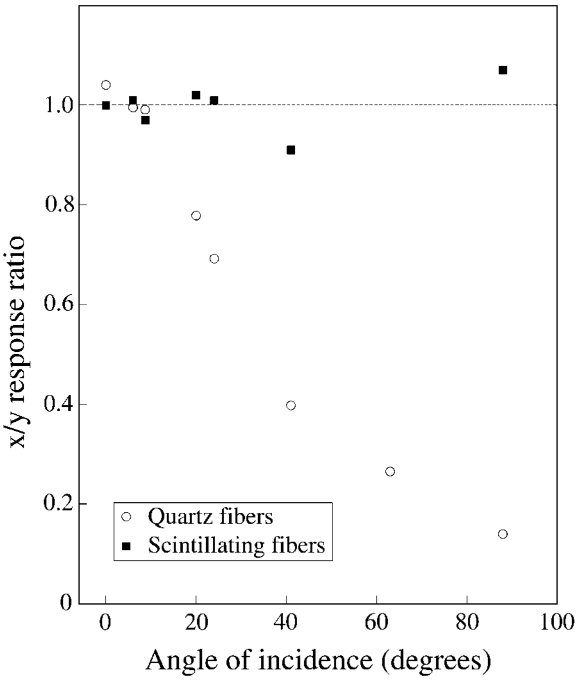

Figure 2: Ratio of the signals measured in fibers oriented in the x and y directions, as a function of the angle of incidence of the showering electrons (200 GeV). Results are shown separately for the quartz fibers and for the scintillating fibers.

Figure 3a, the signals recorded by the quartz fibers are plotted versus those from the scintillating fibers. The non-linear correlation between these signals indicates that they indeed measure different characteristics of the showers.

The scintillator signal distribution, *i.e.* the projection of the scatter plot on the horizontal axis, is shown in Figure 3b. The fact that this distribution is skewed to the low-energy side may be expected as a result of shower leakage. As we argued in Section 1, the relative strength of the quartz signal might be used as a handle on that leakage. For this reason, we investigated the merits of the *ratio of the signals from the quartz fibers and from the scintillating fibers,* Q/S, as an event-by-event measure of the shower leakage.

In Figure 3a, the signal ratio Q/S corresponds to the slope of a line through the bottom left corner of the scatter plot. The two lines drawn in this figure represent $Q/S = 1$ and $Q/S = 0.5$, respectively. On average, the Q/S ratio amounted to 0.77 at 375 GeV. The average value of the Q/S distribution was not very different for the other energies at which we performed our studies. The fact that the Q/S ratio is smaller than 1.0 indicates that a significant fraction, typically 20 - 25%, of the hadronic scintillator signal in this detector was caused by *non-relativistic* shower particles, predominantly protons released from nuclei in spallation processes, or recoiling from elastic neutron scattering in the plastic fibers.

In Figure 3c, the signal distribution is given for events with a small Q/S value ($Q/S < 0.45$). These events indeed populate the left-side tail of the calorimeter's response function (Figure 3b). This distribution is very different from the one obtained for events with Q/S ratios near the most probable value, shown in Figure 3d. The average values of the scintillator signal distributions in Figures 3c and 3d differ by about a factor of two.

These results demonstrate that events from the tails of the Q/S distribution correspond to events from the tails of the (dE/dx) response function. Therefore, we conclude that the ratio of the signals from the quartz and the scintillating fibers does indeed provide information on the energy containment and thus may be used to reduce the fluctuations that dominate the response function of this very thin calorimeter.

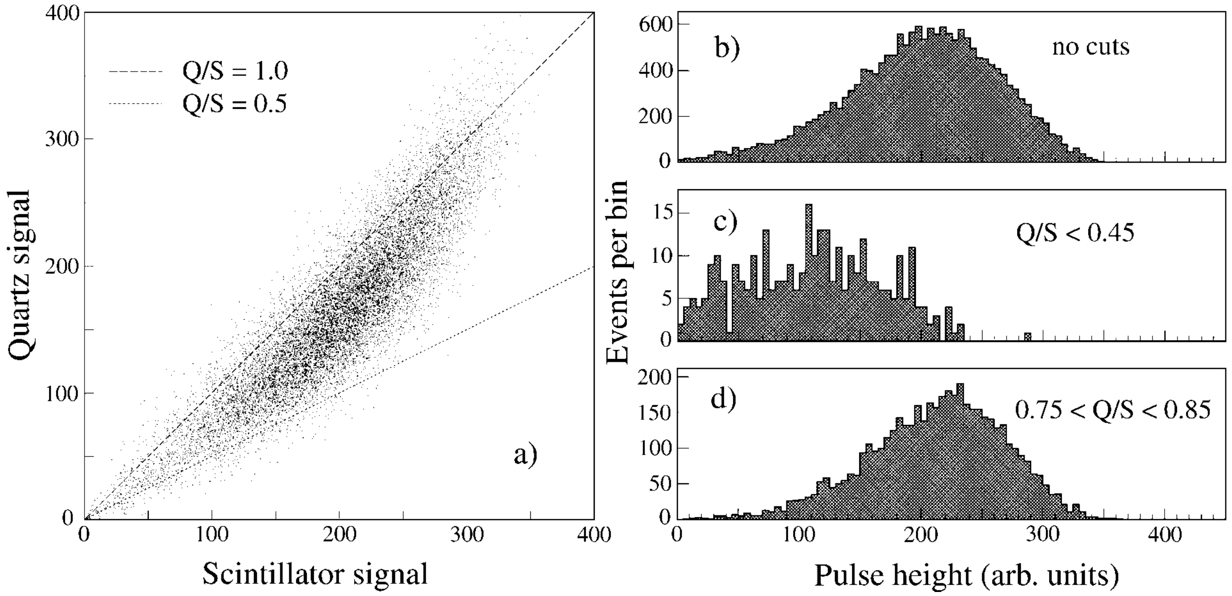

Figure 3: Test results for 375 GeV pions. Scatter plot of the signals recorded in the quartz fibers *vs.* those in the scintillating fibers (a). Signal distributions in the scintillating fibers, for all events (b) and for two subsets of events selected on the basis of their Q/S signal ratio (c, d).

We studied several methods of combining the signals from the two types of fibers and investigated their effects on the response function. The response function could also be improved by removing a small fraction of events with anomalously large or small Q/S values from the event sample. The improvement that could be achieved with such methods turned out to be primarily limited by the light yield of the quartz fibers. Fluctuations in the number of Čerenkov photoelectrons determined the width of the “banana” in Figure 3a and thus the selectivity of Q/S cuts. Therefore, the relative improvement in the energy resolution increased with the hadron energy. This is illustrated in Figure 4, which shows relative improvements in the energy resolution of up to $\sim 15\%$. These results were obtained by cutting 10% of the events from the tails of the Q/S distributions.

Figure 5 shows the fractional width of the distribution of the ratio of the signals from the quartz and the scintillating fibers, represented by the black dots, as a function of the energy of the incoming pions. This energy is plotted on a scale linear in $E^{-1/2}$, so that scaling with $\left[\sqrt{E}\right]^{-1}$ corresponds to a straight line through the bottom right corner of this plot. The experimental data, which cover an energy range of 150 – 375 GeV, are well described by such a line. This means that the width of the Q/S distribution in this energy range is completely determined by fluctuations governed by Poisson statistics, *i.e.* fluctuations in the number of photoelectrons produced by Čerenkov light from the quartz fibers.

As the energy is increased towards the region of interest for the cosmic ray studies, a further improvement of the energy resolution may thus be expected. This trend will continue until the point where factors other than the light yield in the quartz fibers start dominating the width of the Q/S distribution. Since the width of the Q/S distribution continued to improve over the entire energy range accessible in our tests, these experimental data did not allow us to estimate the ultimate improvement in energy resolution that is achievable with our method.

In an attempt to explore these limits, we rearranged the quartz fibers in the detector in such a way that the Čerenkov light from the showers was significantly increased. This was achieved by moving the quartz ribbons from the outermost layers of the detector to the central tower, thus effectively reducing the instrumented surface area from 20×20 cm^2 to 12×12 cm^2. The central tower was also equipped with PMTs with (UV transparent) quartz windows. These

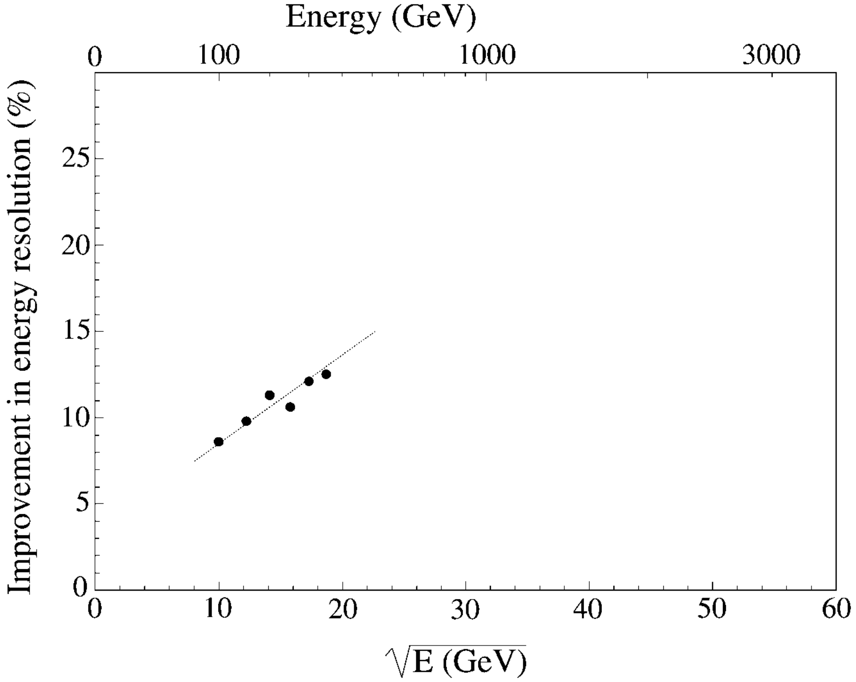

Figure 4: Improvement in the energy resolution for pions as a function of energy.

modifications resulted in an increase of the Čerenkov light yield from 0.5 p.e./GeV to 1.2 p.e./GeV, as determined from the improved resolution for electron showers in the central tower. The width of the Q/S distributions for hadron showers improved accordingly, as illustrated by the black triangles in Figure 5. By increasing the light yield in this way, we effectively extended the energy test range of the original instrument. The fact that the experimental data obtained in this new configuration continued to scale with $[\sqrt{E}]^{-1}$, *i.e.* the fact that also the dash-dotted line in Figure 5 extrapolates to the bottom right corner of the plot, means that the limits of our method to improve the energy resolution by combining Čerenkov and dE/dx information are located beyond this extended reach as well.

However, we did find that the underlying relationship between the signals from the quartz fibers and the scintillating fibers did not change significantly over the energy range accessible in these studies. This relationship was determined by subdividing the $(Q + S)$ spectrum into narrow bins. For each bin, which is represented by a strip oriented perpendicular to the $Q/S = 1$ line in Figure 3a, we determined the average value of the signal from the scintillating fibers. These average values formed the “underlying banana curve”, which gives a precise relationship between the Q/S signal ratio and the fraction of the energy deposited in this calorimeter. This relationship is shown in Figure 6.

This figure shows that the sensitivity and reliability of this method increases as a larger fraction of the shower energy is deposited in the calorimeter. This is no surprise. If an incoming hadron interacts in the calorimeter and produces few or no energetic π^0s, the resulting signals are not very dependent on the energy of the incoming particle, since most of the reaction products escape from the detector. It is, in that case, not well possible to make an accurate estimate of the energy of the incoming particle on the basis of the calorimeter signals. One could, for example, find on the basis of the Q/S ratio that $90 \pm 10\%$ of the shower energy escaped detection. However, that would only set a lower limit to the energy of the showering particle. If, on the other hand, a considerable fraction of the energy of the incoming hadron is converted into π^0s, the Q/S method might lead to quite accurate measurements of the shower leakage.

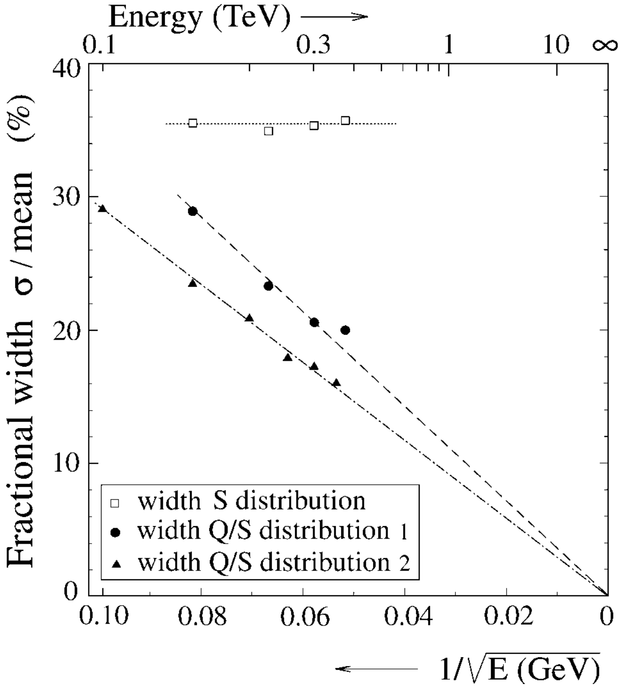

Figure 5: The fractional width of the distributions of the signals from the scintillating fibers S) and of the ratio of the signals from the quartz and the scintillating fibers (Q/S) as a function of the energy. The latter width is given for the original calorimeter configuration (1, black dots) and for a configuration with an increased amount of quartz (2, black triangles).

Consider, for example, a showering 10 TeV hadron that deposits roughly half of its energy in our calorimeter. The quartz signals would in that case consist of 2000–3000 photoelectrons. The experimental uncertainty on the Q/S signal ratio would thus be $\sim 2\%$ for this event. If photoelectron statistics were still the limiting factor at this energy, Figure 6 implies that our method would make it possible to determine the energy of the showering particle with a precision of $\sim 10\%$.

4 Conclusions

We have tested a hadron calorimeter that is based on the novel concept of measuring the properties of the developing showers with two different active media that provide complementary information about the showering particles. By measuring both the scintillation light and the Čerenkov light generated in hadron-induced showers, the energy containment in this very thin detector could be estimated event-by-event. Since fluctuations in the energy containment dominate the performance of this device, this information made it possible to improve the response function, both in terms of energy resolution and in terms of shape, by eliminating non-Gaussian tails.

A crucial parameter in this context turned out to be the ratio of the signals from the two types of fibers, Q/S. Events in which a large fraction of the energy of the incoming particle was spent on π^0 production, and which were thus well contained in the calorimeter, were characterized by a large Q/S value, whereas a small Q/S ratio was indicative for relatively large shower leakage.

We have shown that the beneficial effects of our method were limited by the small light yield of the quartz fibers. We have also shown that the underlying relationship between the signals from both types of fibers, which is responsible

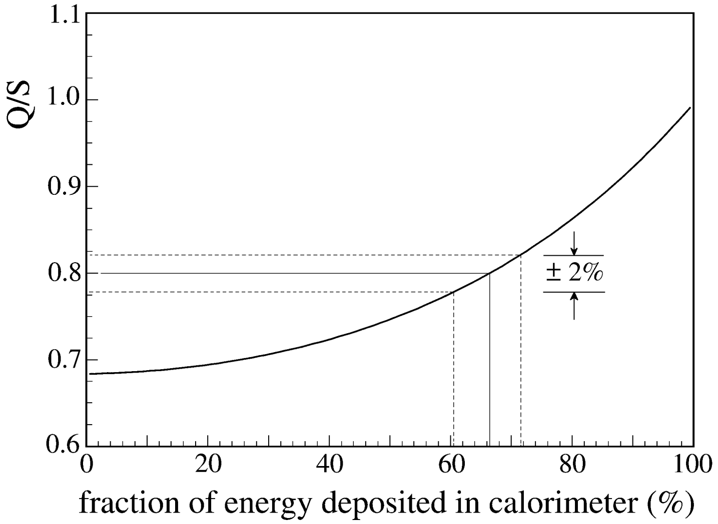

Figure 6: The relationship between the quartz/scintillator signal ratio and the fraction of the hadron energy deposited in the calorimeter.

for the beneficial effects of our method, is independent of energy, at least in the energy range accessible in our test beam experiments. Should this trend continue at higher energies, very substantial benefits of our method may be expected in the multi-TeV energy range for which this device is intended.

Coming back to the needs of limited-mass cosmic ray experiments outside the Earth's atmosphere, we would like to point again to Figure 5. This figure also shows the energy dependence of the hadronic energy resolution measured with the scintillating fibers *alone* (the open squares). This resolution is essentially independent of energy, which illustrates the fact that the light yield of the scintillating fibers is by no means a determining or limiting factor for this resolution. Since the hadronic resolution is completely dominated by fluctuations in shower leakage, a sampling calorimeter with a sampling fraction of less than 0.3% such as this one is thus as good (or bad) for hadron detection as a detector consisting of homogeneously sensitive scintillator material (*e.g.*, bismuth germanium oxide) with the same depth. Only by addressing the fluctuations that *dominate* the resolution, *i.e.* the fluctuations in shower containment, can one hope to improve this performance, as illustrated by the results presented in this paper.

References

[1] N. Akchurin *et al.* , Nucl. Instr. and Meth. **A399** (1997) 202.

[2] R. Wigmans, *Calorimetry – Energy Measurement in Particle Physics*, International Series of Monographs on Physics, Volume 107, Oxford University Press, Oxford (2000).

[3] G. Anzivino *et al.* , Nucl. Instr. and Meth. **A360** (1995) 237.

[4] O. Ganel and R. Wigmans, Nucl. Instr. and Meth. **A365** (1995) 104.

Spectroscopy and Imaging Performance of the Liquid Xenon Gamma-Ray Imaging Telescope (LXeGRIT)

E. Aprile[a], A. Curioni[a], V. Egorov[a], K.-L. Giboni[a], U.G. Oberlack[a],
S. Ventura[a,b], T. Doke[c], J. Kikuchi[c], K. Takizawa[c],
E.L. Chupp[d], P.P. Dunphy[d]

[a]Columbia Astrophysics Laboratory, Columbia University
[b]INFN–Padova, Italy
[c]Waseda University, Japan
[d]University of New Hampshire, USA

ABSTRACT

LXeGRIT is a balloon-borne Compton telescope based on a liquid xenon time projection chamber (LXeTPC) for imaging cosmic γ–rays in the energy band of 0.2- 20 MeV. The detector, with 400 cm^2 area and 7 cm drift gap, is filled with high purity LXe. Both ionization and scintillation light signals are detected to measure the energy deposits and the three spatial coordinates of individual γ–ray interactions within the sensitive volume. The TPC has been characterized with repeated measurements of its spectral and Compton imaging response to γ–rays from radioactive sources such as ^{22}Na , ^{137}Cs , ^{88}Y and Am-Be. The detector shows a linear response to γ–rays in the energy range 511 keV–4.4 MeV, with an energy resolution (FWHM) of $\Delta E/E = 8.8\% \sqrt{1\mathrm{MeV}/E}$. Compton imaging of ^{88}Y γ–ray events with two detected interactions is consistent with an angular resolution of $\sim$ 3 degrees (RMS) at 1.8 MeV.

Keywords: gamma-rays, instrumentation, imaging, telescope, balloon missions, high energy astrophysics

1. INTRODUCTION

Progress in MeV γ–ray astrophysics has lagged far behind that in the X–ray band and at high energies, because of the difficulty of imaging MeV photons combined with the high background and the low cosmic source fluxes. Results from CGRO–COMPTEL,[1] the only Compton Telescope in space to-date, have shown both the promise and the challenges of this field. To explore the rich scientific potential of this energy band, new instruments are needed which combine substantially higher detection efficiency and background rejection capabilities, within a large field-of-view.

The development of a liquid xenon time projection chamber (LXeTPC) at Columbia was initiated to demonstrate the feasibility of the technique and to study its capability as efficient Compton telescope for MeV γ–ray astrophysics. The combination of calorimetry and 3D event imaging in a TPC is especially powerful for reconstructing the multiple Compton histories of MeV γ–rays, and thus the incoming direction and energy on an event-by-event basis. Equally important, the imaging capability proves to be a powerful tool in rejecting background. After the characterization in the laboratory, the LXeTPC has been turned into a balloon-borne instrument (LXeGRIT) to test its performance in the near space environment. A description of the instrument and its performance during its May 1999 balloon flight in New Mexico are reported elsewhere in these proceedings.[2] Here we present some of the results on the detector spectral and imaging performance, obtained during the pre-flight calibration experiments with radioactive sources of gamma-rays at energies between 511 keV and 4.4 MeV.

2. THE LXETPC AS γ-RAY SPECTROMETER AND COMPTON IMAGER

A schematic of the LXeTPC and its principle of operation is shown in Fig. 1. The TPC is assembled in a cylindrical vessel of 10 l volume, filled with high purity LXe at a temperature of $\sim -100^\circ$ C. The sensitive area is 20×20 cm^2 and the maximum drift length is 7 cm. The detector operates over a wide energy range from $\sim$ 200 keV to 20 MeV.

Send correspondence to: E. Aprile, Columbia University, Astrophysics Laboratory, 550 West 120th Street, New York, NY 10027
E-mail: age@astro.columbia.edu
LXeGRIT Web page: `http://www.astro.columbia.edu/~lxe/lxegrit/`

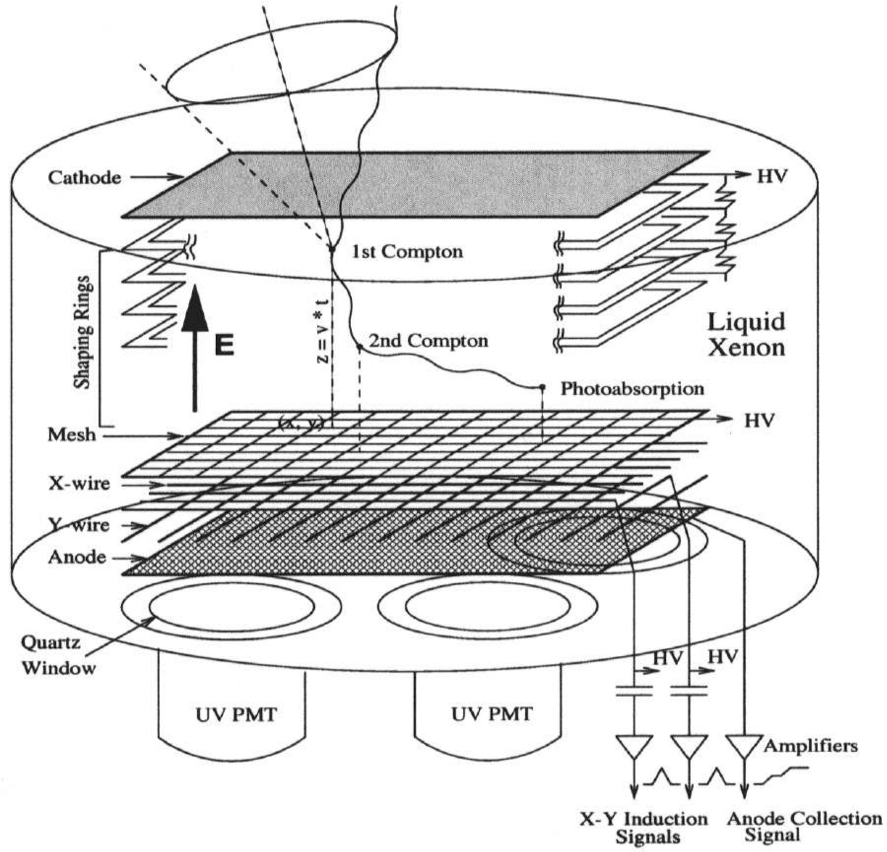

Figure 1. LXeTPC schematic.

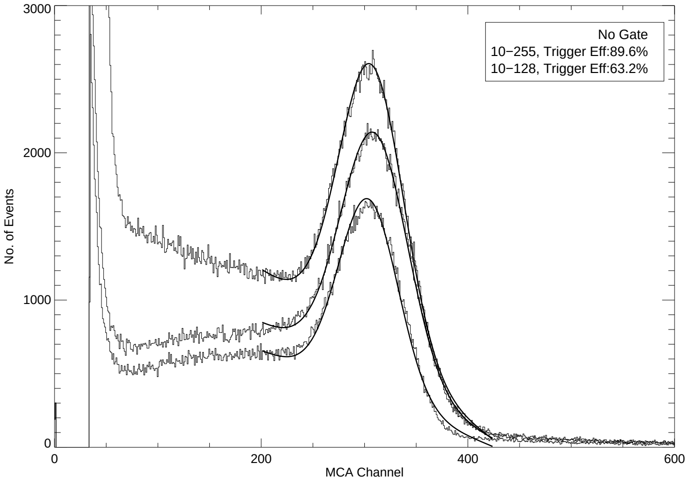

Figure 2. ^{137}Cs 662 keV energy spectra for all anode signals (*upper curve*) and for anode signals with a light trigger (*lower curves*) for two discriminator windows.

2.1. Light signals detection and processing

Both ionization and scintillation light signals, produced by a charged particle in the liquid, are detected to measure its energy and 3D position. The fast ($<$ 5 ns) Xe light (175 nm), detected by four UV sensitive photomultiplier tubes (PMTs) coupled to the detector vessel by quartz windows, provides the event trigger. The signals from the PMTs are passed trough a set of window discriminators: the lower threshold of the discriminators avoids triggering the readout on noise pulses, while the upper threshold reduces the number of high-energy charged particle events. The choice of the upper and lower threshold, together with the PMTs high-voltage, impacts significantly the detector's trigger efficiency.

The light level seen by the PMTs is extremely low. The total number of photons produced in LXe by a charged particle is reduced by the quenching of the recombination luminescence due to the applied electric field. More photons are lost due to geometrical effects (solid angle), low reflectivity of the chamber materials, optical transmission of the wires and anode meshes and transmittance by the quartz windows. The efficiency of each PMT was estimated by measuring the count rate of the triggering events relative to the total count rate. This was done by comparing the Multi Channel Analyser (MCA) spectrum of the charge signals from the anode directly above the PMT, gated by the PMT light trigger and ungated. The ratio of events with a trigger and of all events, under the full energy peak, was taken as the trigger efficiency for the particular γ-ray energy line. Three spectra for a collimated ^{137}Cs source, placed above the center of one anode, are shown in Fig. 2. The voltage on the corresponding PMT was 1800 V. The MCA spectra were taken with 10 μs shaping time for the anode shaping amplifier. Given the 35 μs maximum drift time, γ-rays interacting two or more times in locations more than 10 μs apart in drift time contribute to the background below the line. From a fit of the lines, the trigger efficiency at 662 keV is 89.6 % for the discriminator window of 10–255. By lowering the upper threshold from 255 to 128, the efficiency drops to 63 %.

2.2. Charge signals detection and processing

The drift of free ionization electrons in the LXeTPC uniform electric field, typically 1 kV/cm, induces charge signals on a pair of orthogonal planes of parallel wires with a 3 mm pitch, before collection on four independent anodes (see Fig. 1). Each of the 62 X-wires and 62 Y-wires and each anode is amplified and digitized at a sampling rate of 5 MHz, to record the pulse shape. The X-Y coordinate information is obtained from the pattern of hits on the wires, while the energy is obtained from the amplitude of the anode signals. The Z-coordinate is determined from the drift time measurement, referred to the light trigger. For a review of the TPC signal characteristics and their electronics readout we refer to Aprile et al. 1998.[4] The system is such that the equivalent noise charge on the wires is typically less than $\sim$ 400 e$^-$ RMS, while the noise on the anodes, of higher capacitance, is $\sim$ 800 e$^-$ RMS. With these noise conditions, the TPC can well detect the multiple interactions of MeV γ–rays, with a minimum energy deposit of $\sim$150 keV.

Fig. 3 shows the TPC display of a ^{88}Y 1.8 MeV γ–ray event. The digitized signals on all wires and active anodes are shown as a function of drift time. The incoming photon makes two Compton scatterings befor being photoabsorbed. In this "3–steps" event, in fact, the sum of the three anode pulse heights gives 1.8 MeV. The corresponding location of the interactions are clearly seen on the X-Y wires. An efficient and fast signal recognition algorithm has been developed to sort the different event topologies and to obtain the energy and X-Y-Z coordinates from the digitized signals of each interaction recorded in the sensitive volume.[3] With this information, and with the gain and energy calibration curves, spectral and imaging analysis of gamma-ray sources is then carried out.

2.3. Energy Resolution and Calibration

The response of the TPC to γ–rays was characterized in several experiments with the electronics, trigger conditions and data acquisition system as used during the May 99 flight. The following radioactive sources were used: ^{137}Cs , ^{22}Na and ^{88}Y with lines at 662 keV, 511 keV and 1275 keV, 898 keV and 1836 keV, respectively. The sources were either collimated or placed at some distance (2–4 meters) from the TPC. Data were also taken with an Am-Be neutron source, which emits 4.43 MeV gamma-rays, as well as with cosmic rays.

For detectors with a large drift region like LXeGRIT, the Xe purity largely determines the charge yield and thus the spectral response. To minimize the charge loss due to attachment of free electrons to electro-negative impurities, an efficient purification system was developed and has been fully discussed in Xu 1998.[6] The simple relation

$$Q_{det} \;=\; Q_0 \cdot exp(-\frac{z}{\lambda_{att}}) \tag{1}$$

describes the detected charge Q_{det}, given an initial charge Q_0 at a distance z from the collection point. The parameter λ_{att} is the attenuation lenght for electrons drifting in liquid Xe. If not corrected, even a modest (few percent) dependence of the collected charge on z would deteriorate the energy resolution.

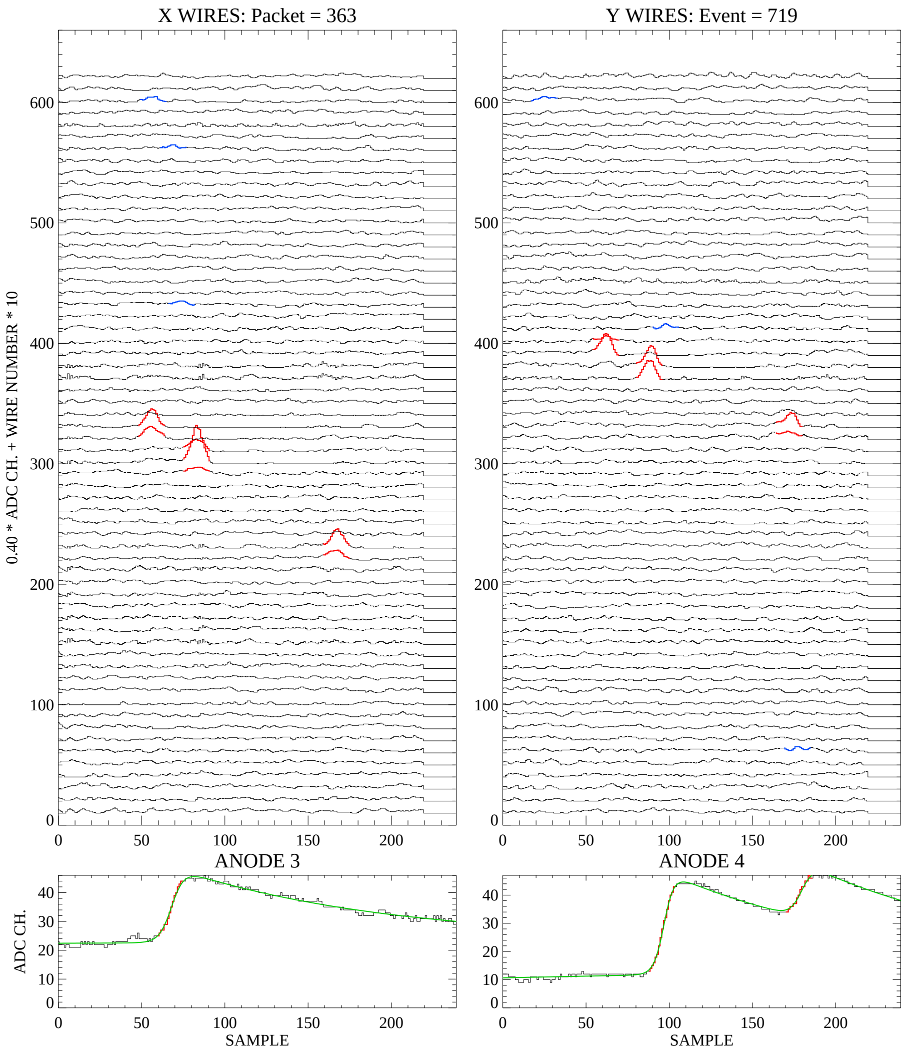

Figure 3. LXeGRIT on-line display of a 1.8 MeV γ-ray event with multiple Compton interactions.

The measurement of the absolute depth of an interaction in the light triggered LXeTPC offers a direct method to infer the drifting electron lifetime and thus the purity of the LXe. Given a γ–ray line, in this case 662 keV, the procedure consists in measuring the photopeak amplitude for different *z* (i.e. drift time) slices, as shown in Fig. 4. The photopeak dependence *vs.* *z* is then fitted with the relation 1 to yield λ_{att}, i.e. the electron lifetime. The scatter plot of the amplitude of the ^{137}Cs events *vs.* drift time at 1 kV/cm is shown in Fig. 5, for single interaction events. The enhancement seen in correspondence to the 662 keV full energy peak moves to lower pulse heights for longer drift time. The measured drifting electron lifetime is about 360 μs: this lifetime corresponds to an attenuation lenght of 80 cm, to be compared with the 7 cm maximum drift lenght in our detector. A correction for attachment to impurities is applied during event reconstruction on an event-by-event basis, removing the dependence of the signal amplitude on the distance from the anode and so significantly improving the spectral performance.

The spectral performance of the LXeTPC, inferred from the analysis of either single or multiple interaction events, is shown with the reconstructed energy spectra of the ^{22}Na , ^{137}Cs , ^{88}Y and Am-Be sources (see Figs. 6, 7, 8, 9).

Fig. 6 shows the 511 keV energy spectrum measured with a tagged ^{22}Na source: ^{22}Na simultaneously emits a 1275 keV γ–ray plus a positron, promptly annihilating and producing two 511 keV γ–rays in opposite directions, so that one of the two 511 keV photons can be used to tag the other one, reducing 1275 keV and pile-up events. In our case, when 511 keV energy deposit was detected in a NaI(Tl) scintillation counter placed above the TPC, a trigger was sent to the TPC.

Fig. 7 shows the energy spectrum of a collimated ^{137}Cs source. In both cases, we point out the large enhancement of the *peak-to-Compton-ratio* obtained with multiple interactions events, compared to the single interaction events spectrum.

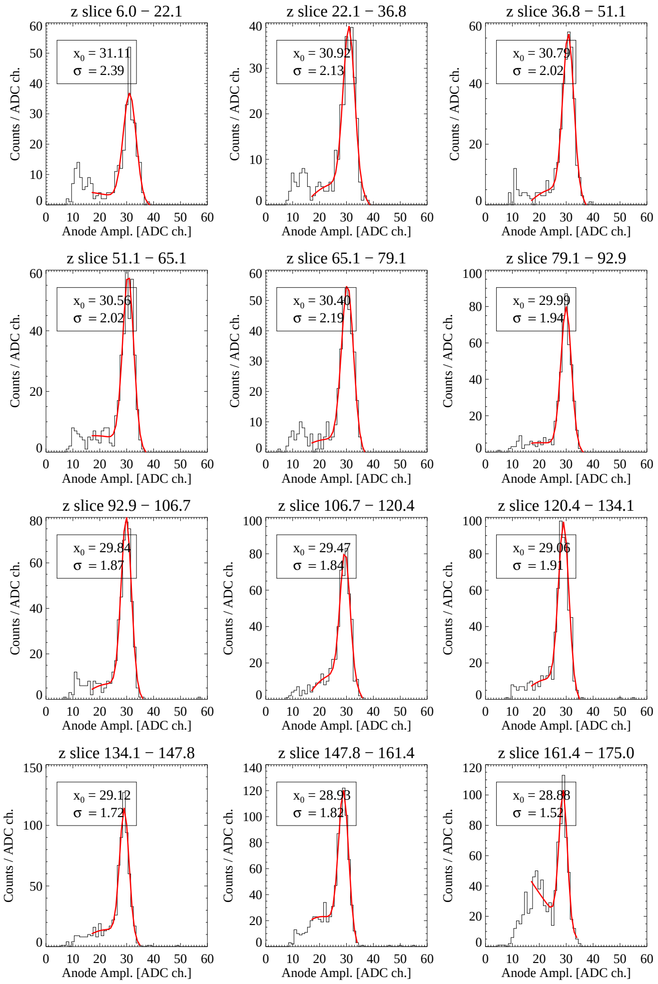

Figure 4. ^{137}Cs (collimated source) energy spectra for different drift times: each "slice" of the fiducial volume is 6 mm thick. Going from top to bottom the drift time increases.

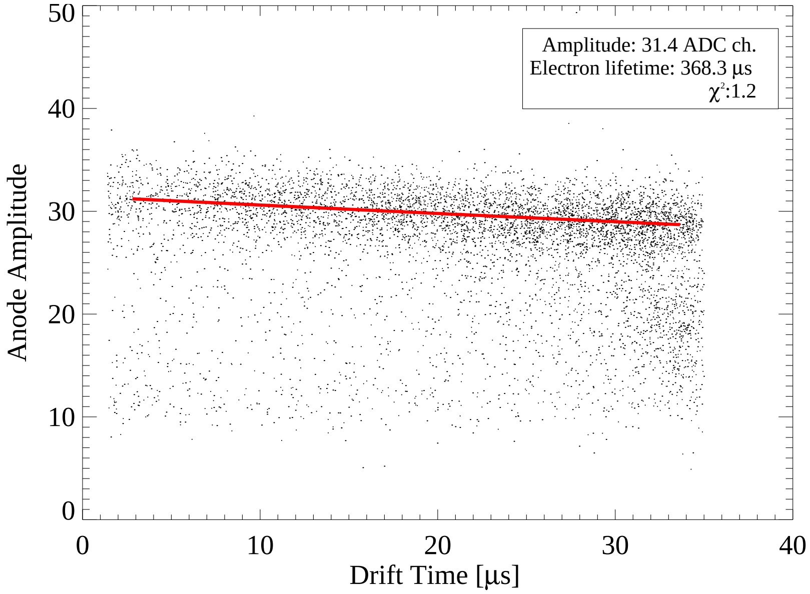

Figure 5. Anode amplitude (ADC ch.) *vs.* drift-time (*μ*s). Drift-time is directly converted in *z*-position. The solid line is the result of an exponential fit to the photopeak position for various slices in drift time.

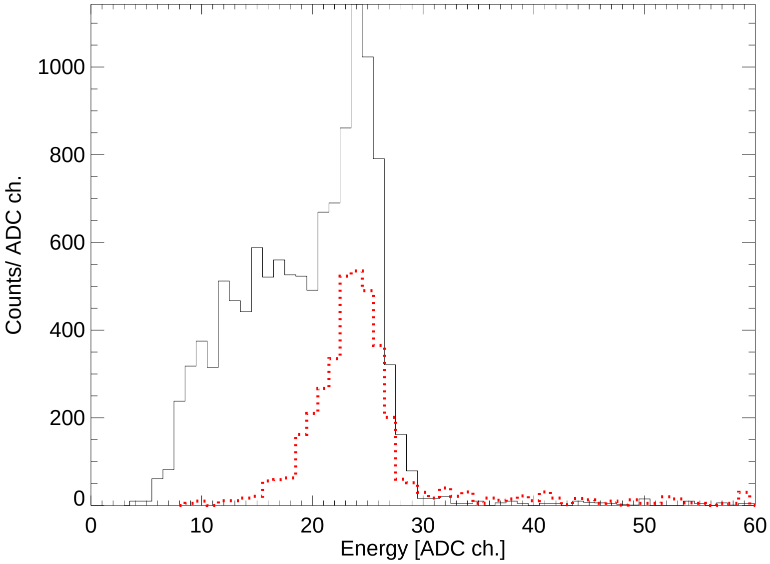

Figure 6. ^{22}Na 511 keV energy spectrum for single interaction (*solid line*) and Compton interaction events (*dotted line*). Note the suppression of the Compton continuum and the large enhancement of the peak-to-Compton ratio in the multiple interactions sample.

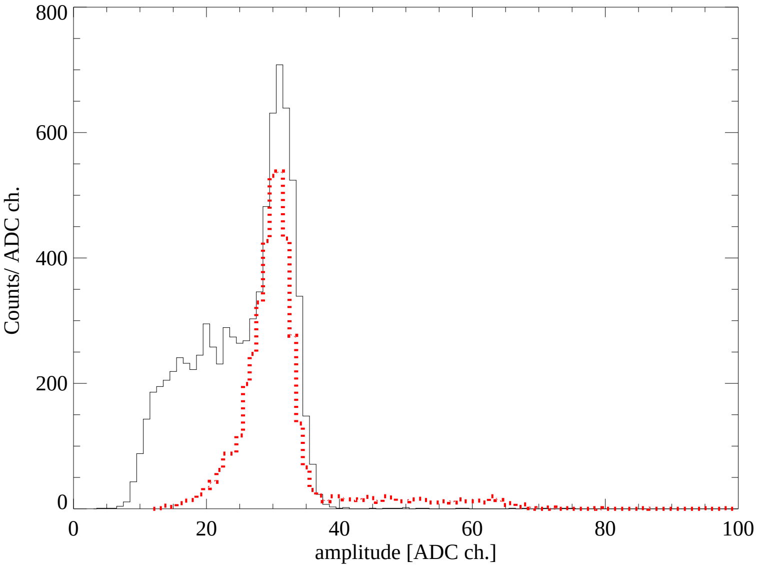

Figure 7. ^{137}Cs 662 keV energy spectrum for single interaction (*solid line*) and Compton interaction events (*dotted line*). Note the suppression of the Compton continuum and the large enhancement of the peak-to-Compton ratio in the multiple interactions sample.

Fig. 8 shows the ^{88}Y energy spectrum obtained from events with two interactions (”2–step” events). In this experiment the source was placed about 2 m above the TPC to simulate a parallel γ-rays beam for imaging analysis, as discssed in the next section. Aside the 898 and 1836 keV photopeaks, the single escape peak (1325 keV) for 1836 keV photons is detected. Fig. 9 shows the energy spectrum from an Am-Be neutron source. Again ”2–step” events were used. Since the cross-section for pair-production is large at 4.4 MeV, the single escape peak (3.92 MeV) is prominent. Photopeak, single and double (detected in the “1-step” events spectrum, not shown here) escape peaks and the Compton edge have been used in the energy calibration.

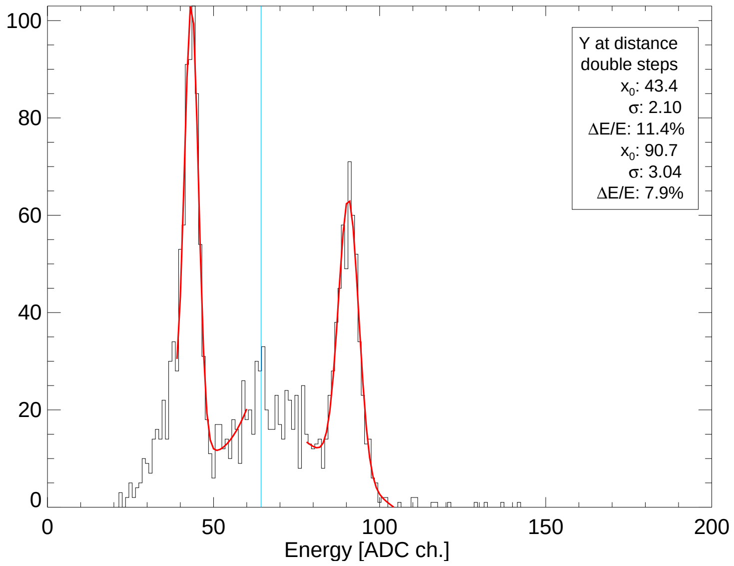

Figure 8. ^{88}Y 898 keV and 1836 keV energy spectrum for two interaction (”2–step”) events. The source was placed about 2 m above the TPC.

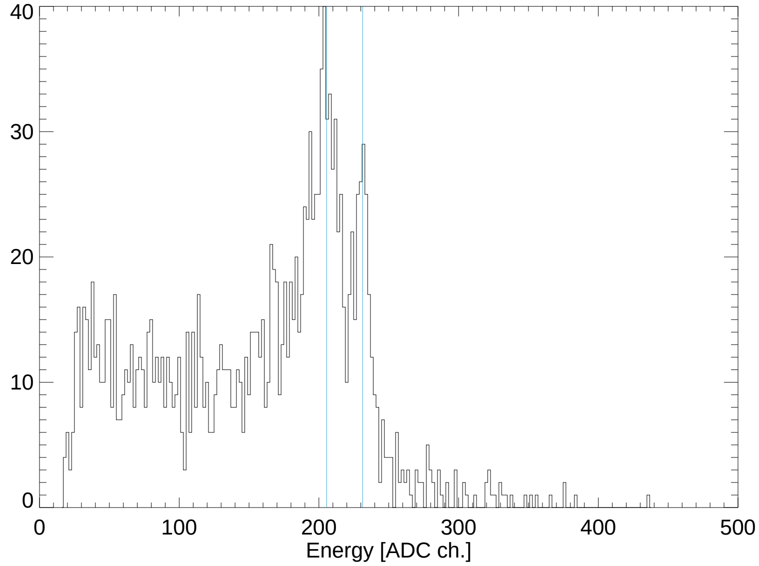

Figure 9. Am-Be energy spectrum for two interaction (”2–step”) events. The photopeak (4.43 MeV) and the single escape peak (3.92 MeV) are clearly identified.

The calibration curve obtained combining the ^{137}Cs , ^{22}Na , ^{88}Y and Am-Be data is shown in Fig. 10. The non linear term is small, indicating good proportionality over the energy range 511 keV– 4.43 MeV. The energy resolution of all the lines is consistent with a value of 10 % (FWHM at 1 MeV), scaling as $1/\sqrt{E}$. This value includes electronics noise, shielding inefficiency and non linearities in the gain response due to the electronics as well as the signal processing analysis. The noise subtracted energy resolution is 8.8 % (FWHM at 1 MeV) (see Fig. 11), in excellent agreement with expectations.

2.4. Compton Imaging and Angular Resolution

To test the Compton imaging performance of the telescope, the LXeTPC was irradiated with a parallel beam of γ–rays from a ^{88}Y calibration source placed at a distance of several meters. Here we present the results obtained with γ–ray events, for which two interactions are recognized in the sensitive LXe volume (”2–step” events). Events with a single

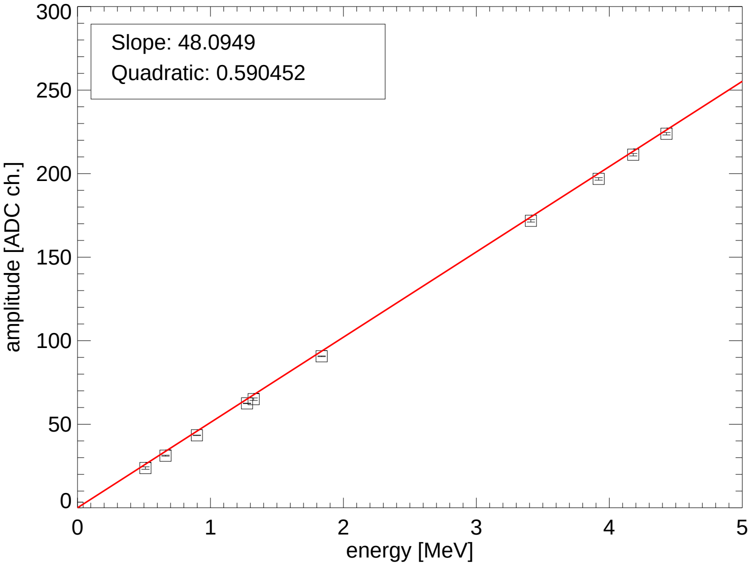

Figure 10. Energy calibration curve for one of the four LXeTPC anodes: anode amplitude *vs.* energy fitted with $amp = b \cdot E + c \cdot E^2$. In the inlet, b = "slope" and c = "quadratic".

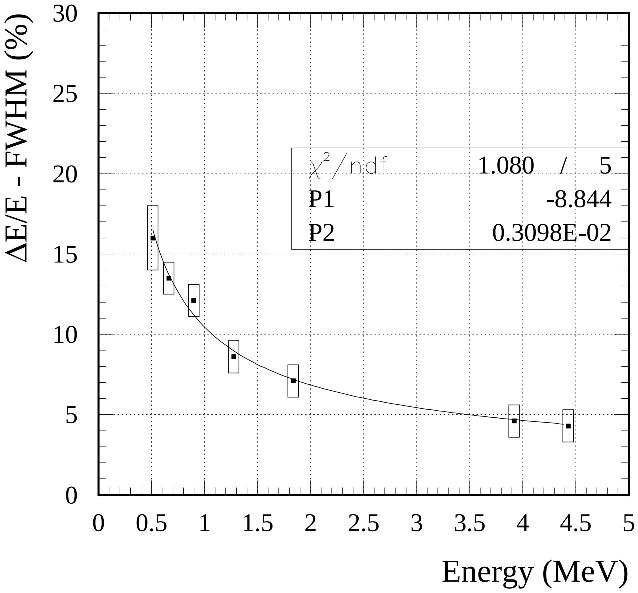

Figure 11. Energy resolution *vs.* energy: $\Delta E_{\mathrm{lxe}}/E = 8.8\% \sqrt{1\mathrm{MeV}/E}$

Compton scattering followed by a photoabsorption are the simplest ones that can be used for imaging a source at a known location. The process of determining the imaging response breaks down into three parts:

1. Energy calibration, which is necessary for the relation of charge deposits to the electron mass m_0c^2 in the calculation of the Compton scatter angle $\bar{\varphi}$ (equation 3). This includes correction for charge losses due to electron attachment according to the depth of the interaction (z-position), as described in section 2.3. The conversion from ADC counts

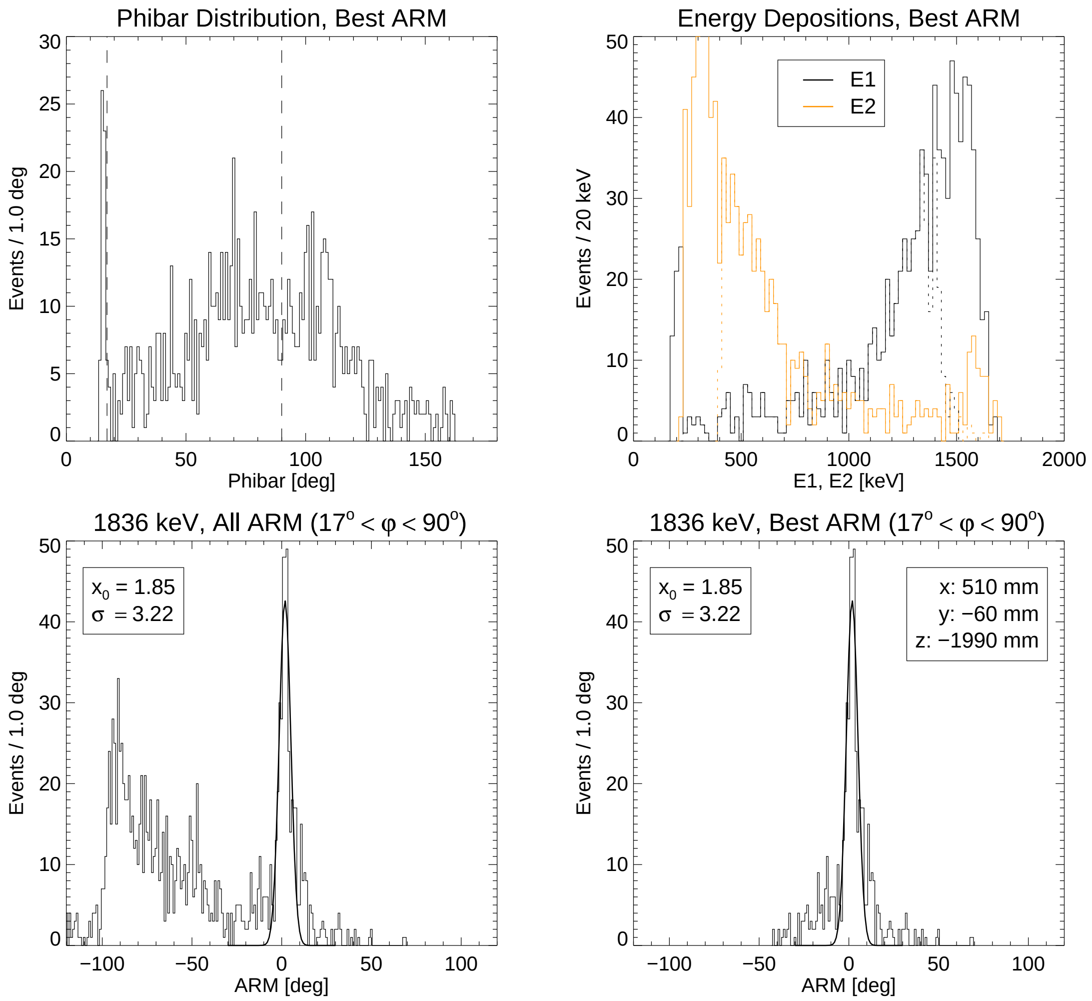

Figure 12. *Top left:* $\bar{\varphi}$ distribution for two-step events in the full energy peak of the 1836 keV ^{88}Y line. *Top right:* energy deposit in each interaction. *Bottom:* ARM spectra for two-step events in the full energy peak of the 1836 keV ^{88}Y line.

to keV is then based on the four anode calibration curves, such as that of Fig. 10.

2. Determination of the time sequence of the two interactions. For events with two interactions, the LXeTPC provides no redundant measurement that would uniquely determine the interactions sequence. In the case of calibration data with known source position, the sequence with the minimum value of "angular resolution measure" (ARM) as defined below, can be chosen. For data with unknown source location, the decision on the correct sequence can be based on a maximum energy value assigned to the second step, since the photo-absorption cross section falls off steeply beyond 200 keV in xenon (see[7,8] for similar approaches). Alternatively, both sequences might be used in a likelihood analysis, which uses relative probabilities for each sequence with respect to a source position. Such extended instrumental response would be derived from Monte Carlo simulations.

3. Derivation of the ARM distribution, i.e., the distribution of scatter angles $\bar{\varphi}$ derived from Compton kinematics minus the geometrical scatter angles $\varphi^{\triangleleft}$ between the known source position and the measured scatter direction, given by the two interaction locations:

$$ARM = \bar{\varphi} - \varphi^{\triangleleft} \tag{2}$$

$$\cos\bar{\varphi}_{ij} = 1 - \frac{m_0c^2}{E_j} + \frac{m_0c^2}{E_i + E_j} \qquad i, j = \{1,2\} \text{ or } \{2,1\} \tag{3}$$

$$\cos\varphi^{\triangleleft}_{ij} \;=\; \frac{\vec{r}_{ij}\cdot\vec{r}_{\star i}}{|\vec{r}_{ij}|\,|\vec{r}_{\star i}|} \qquad (4)$$

E_i, E_j denote the energy deposits presumed to be first and second, respectively. $\vec{r}_{ij} = \vec{r}_j - \vec{r}_i$ is the vector between the locations i, j and $\vec{r}_{\star i}$ is the vector between the source and location i.

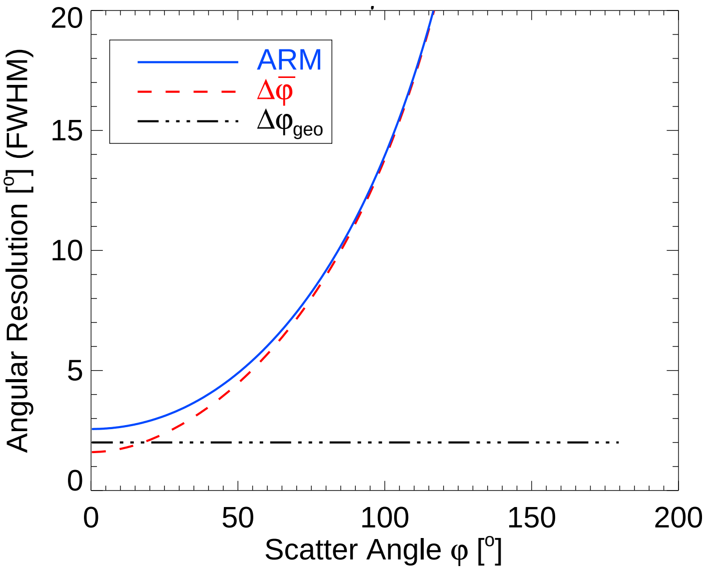

Figure 13. Angular resolution (ARM) *vs.* $\bar{\varphi}$ for 1.8 MeV photons (solid line) and contributions from energy resolution (dashed line) and position resolution (dash-dotted line).

For a γ-ray line source, as is the case for our calibration data, events can be restricted to the full-energy peak, i.e., amplitudes $A_1 + A_2 \approx A_{\rm line} \pm 2\sigma$. The ^{88}Y energy spectrum with the two lines at 898 keV or 1836 keV as obtained from two-step events was previously shown in Fig. 8 Also, we require $\cos\bar{\varphi} \geq -1$ for a valid Compton sequence. Invalid sequences can result in $\cos\bar{\varphi}$ values < -1. In fact, true Compton sequences with large scatter angles, can also yield $\cos\bar{\varphi}$ values < -1, due to the energy uncertainty of the measurement. Back-scattered events would be rejected in any case since they provide a poor imaging response. Results from the analysis of 1836 keV "2-step events" from ^{88}Y at a distance of about 2 m and at a zenith angle of $\sim 25°$ are shown in Fig. 12. The *Top left* panel shows the $\bar{\varphi}$ distribution for events in the full energy peak. The *Top right* panel shows the distribution of the energy deposit in each interaction. The *Bottom left* panel shows the ARM distribution of the events in the full energy peak, derived without selecting a time sequence, while the sequences with the smaller ARM value for a given source position was selected for the *Bottom right* panel. The ARM values for the two sequences are sufficiently separated, with the false sequence assuming a maximum around $-93°$, such that choosing the smaller ARM, in the *Bottom right* figure, does not bias the ARM peak for the correct sequence. The imaging response for these two-step events consists of a narrow peak of 3.3° (1σ) for a scatter angle selection of $17° < \bar{\varphi} < 90°$. This angular resolution value is consistent with expectations, as shown in Fig. 13: for a scatter angle of 70° the resolution is about 7° (FWHM) at 1.8 MeVṪhe expected LXeGRIT angular resolution for a γ-ray line at 1.8 MeV shown in in this figure was calculated based on the experimental energy resolution (FWHM) of $\Delta E/E = 10\% \sqrt{1{\rm MeV}/E}$ and assuming a 2° geometrical angle contribution due to the uncertainty in the position measurement.

The non-Gaussian wings in the measured ARM distribution may be due to three-interaction events that are seen as two steps within the resolution of the detector, or to imperfections in the off-line fitting of the anode waveform. Note that with a minimum spatial separation of ~ 2 cm between the two interactions, the angular response is fully determined by the energy resolution and by the lowest energy threshold, which in this data set was about 170 keV. This imposes an energy-dependent lower threshold in $\bar{\varphi}$. For events with three or more interactions, the correct sequence of scatterings can be inferred from the redundant position and energy information measured by the TPC for each interaction. The performance of a Compton sequence reconstruction algorithm on LXeGRIT "3-step" events is reported in Oberlack et al. 2000.[9] In this paper we show that the ARM distribution for the 1836 keV line of ^{88}Y events has a width of $\sim 3°$ (1σ), consistent with the result obtained with the "2-step" events.

3. CONCLUSIONS

During 1999 the spectral and imaging performance of the LXeGRIT instrument was extensively measured with a variety of γ–ray sources, spanning the energy range 511 keV–4.4 MeV, in preparation for the May '99 balloon flight. Results can be summarized as follows:

- the LXeTPC energy response shows a good linearity over the measured. energy range

- the LXeTPC energy resolution, at an electric field of 1kV/cm, is 8.8% FWHM at 1 MeV scaling with $1/\sqrt{E}$. This value is consistent with previous results, obtained however with simple gridded ionization chambers with drift regions of a few mm to a few cm (see for example Aprile et al. 1991[10]).
- the 3D imaging capability of the TPC has been confirmed as a powerful tool to suppress background events and to enhance the *peak-to-Compton ratio* in the measured spectral distributions.
- the TPC works as a Compton telescope: γ–ray sources can be imaged with an angular resolution consistent with expectations (3 $^\circ$ RMS for 1.8 MeV γ–rays).
- the overall performance of the TPC in the laboratory shows excellent stability in time, from the liquid purity to the high voltage, from the cryogenics to the analog and digital electronics.

These results confirm the applicability of this new detector concept to MeV γ–ray astrophysics.

ACKNOWLEDGMENTS

This work was supported by NASA under grant NAG5-5108.

REFERENCES

1. Schönfelder V., et al., 1993, ApS 86, 657
2. Aprile E., et al., 2000, SPIE Conference Proceedings, Vol. No. 4140
3. Oberlack U.G. et al., in preparation
4. Aprile E., et al., 1998. NIM A 412, 425
5. Aprile E., et al., AIP Conference Proceedings, No. 510, p. 799, 2000
6. Xu F., Ph.D. Dissertation Thesis, Columbia University, 1998
7. Boggs, S. E. and Jean, P., 2000, A&AS, in press (astro-ph/0005250)
8. Schmid, G. J., et al., 1999, NIM A 430, 69
9. Oberlack U.G. et al., 2000, SPIE Conference Proceedings, Vol. No. 4141
10. Aprile E., et al., 1991. NIM A 302, 177

February 2, 2001

OPTICAL PROPERTIES OF THE DIRC FUSED SILICA CHERENKOV RADIATOR

J. Cohen-Tanugi, M. Convery, B. Ratcliff, X. Sarazin, J. Schwiening, and J. Va'vra*

Stanford Linear Accelerator Center, Stanford University,
Stanford, CA 94309, USA

ABSTRACT

The DIRC detector is successfully operating as the hadronic particle identification system for the BaBar experiment at SLAC. The production of its Cherenkov radiator required much effort in practice, both in manufacture and conception, which in turn required a large number of R&D measurements. One of the major outcomes of this R&D work was an understanding of methods to select radiation hard and optically uniform fused silica material. Others included measurement of the wavelength dependency of the internal reflection coefficient, and its sensitivity to the surface pollution, selection of the radiator support, selection of good optical glue, etc. This note summarizes the optical R&D test results.

1. INTRODUCTION

The Detector of Internally reflected Cherenkov light (DIRC) [1] is a new type of Cherenkov ring imaging detectors, which has been operating successfully at the BaBar experiment at SLAC for over one year. The device uses synthetic fused silica bars (colloquially called synthetic quartz), which serve both as the Cherenkov radiator and as light guides transmitting the photons to an array of ~11,000 photomultiplier tubes (PMT). A fraction of the Cherenkov photons produced by tracks passing through the bars are trapped by total internal reflection and propagate down the bar with very little loss. A mirror at the far end reflects those photons that were originally traveling away from the detection end of the bar. At the end of the bar, photons pass through a fused silica wedge, which reflects those photons that would otherwise miss PMTs. Then photons pass through a window, which separates the box holding the bars from water. Water is the optical coupling medium between the bars and the PMT detector. The distance between the bar box window and the PMT detector is about 1.2 m. Figure 1 shows the photon path as it leaves a five-meter long fused silica bar.

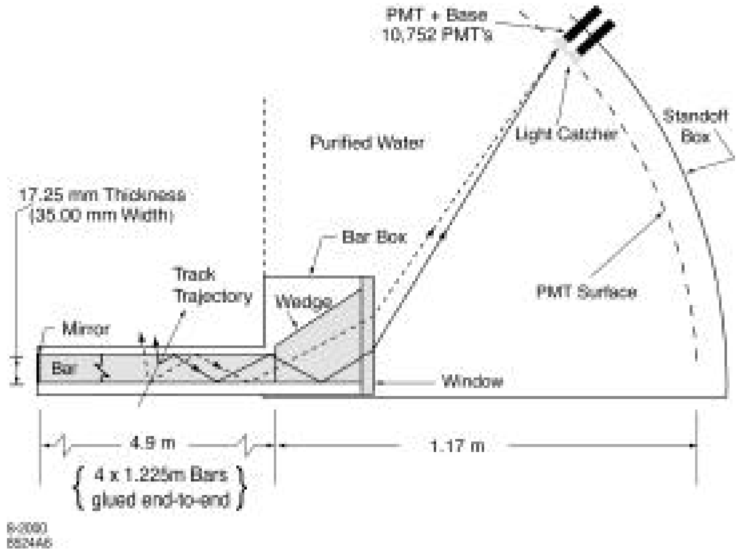

Figure 1. Imaging of Cherenkov photons with DIRC fused silica bar. A wedge at the end of each bar allows the proper placement of the image within the photon detector, which is made with ~11000 PMTs.

---

* Work supported by the Department of Energy under contract DEAC005SF1

Figure 2 shows a single bar box with 12 bars. Within the bar box, each bar measures ~5 m in length and is made of four short segments glued together with EPOTEK 301-2 optical epoxy.[1] Each short segment has the following design specifications: length 1225.0 mm, width 35.0 mm, and thickness 17.2 mm. To preserve the image resolution and timing properties, the original specification was that any bar face-to-side angle to be within ±0.25mrad of 90^o (see chapter 7 for a final compromise). The bars must have sharp edges without too many chips to limit photon losses (specifications required for less than $6mm^2$ of damaged surface per bar). To check that the mechanical specifications are within our tolerances, we have built our own digital microscope system and developed our own image reconstruction software. Since the trapped Cherenkov photons must typically bounce several hundred times before they exit the bar, the internal reflection coefficient must be close to one. A reflectivity coefficient of less than 0.999 is unacceptable. Losses as small as 10^{-4} per bounce must be measured. Since such small losses are difficult to measure in a single bounce, we have developed a new method to measure the reflection coefficient by combining ~50 bounces in a single measurement. The high value of surface reflectivity has to be maintained for expected ten-year lifetime of the experiment. Therefore, we studied a possible influence of fused silica surface pollution on the reflectivity coefficient. Another important factor is the bar transmission and its uniformity. Similarly, a problem of fused silica support within a bar box was a good subject for the R&D tests. In addition, it was important to select radiation hard fused silica and optical glues. This is because the BaBar detector operates at a high luminosity machine (PEP II presently operates at a luminosity of $\sim 3x10^{33}$ $cm^{-2}sec^{-1}$ and it is planned to go beyond 10^{34} in one to two years).

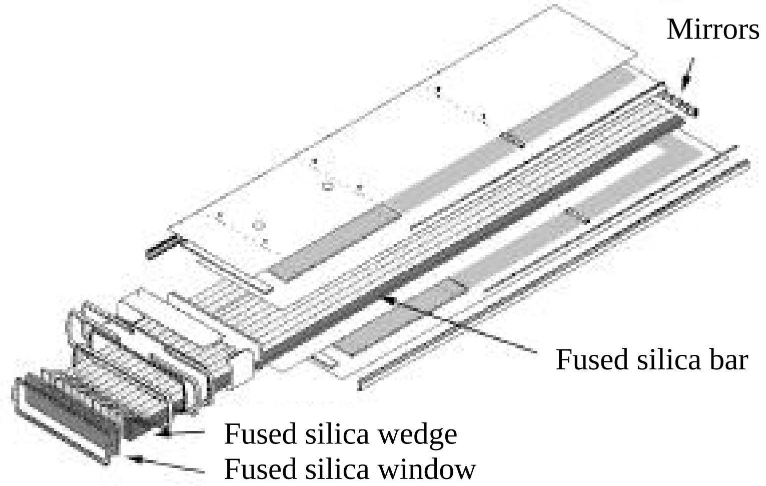

Figure 2. DIRC fused silica Cherenkov radiator as implemented in the BaBar experiment at SLAC. Twelve 5-m long fused silica bars are located in each bar box. There are 12 such bar boxes in the DIRC detector.

2. BASIC PROPERTIES OF FUSED SILICA

2.1. Refraction Index

To account for various effects in the DIRC, it is necessary to know the refraction index of water, fused silica, and EPOTEK 301-2 optical glue used for gluing the bars. Figure 3 shows the refraction index for fused silica [2] and water [3]. Figure 4 shows the calculated reflection coefficients at incidence angle of 0^o for the boundaries of fused silica/water and fused silica/EPOTEK 301-2 [4]. Due to a good match of the fused silica and glue refraction indices, the reflection coefficient is small (less than 0.15%) and almost independent of wavelength above 300nm.

---

[1] Made by Epoxy Technology Inc., 14 Fortune Drive, Billerica, MA 01821, USA.

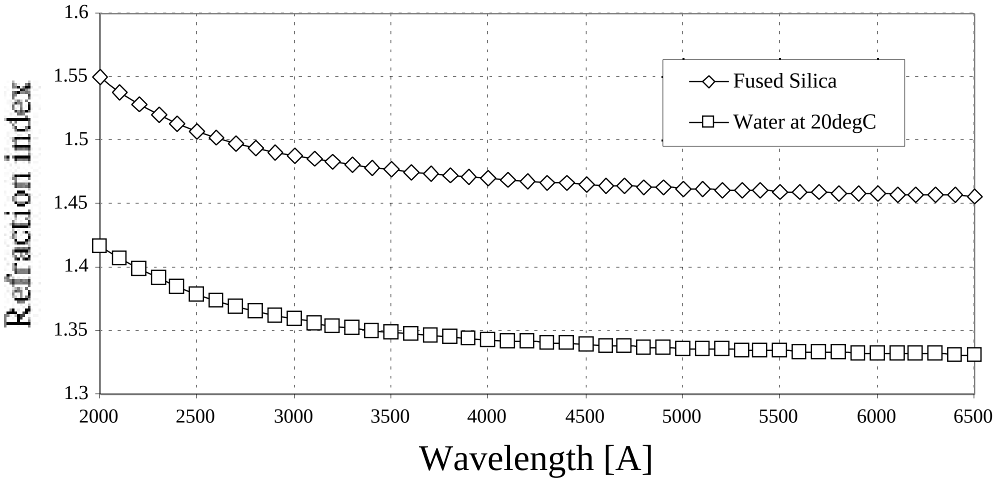

Figure 3. Wavelength dependence of the refraction indices for fused silica and water. The DIRC acceptance starts at 3000Å.

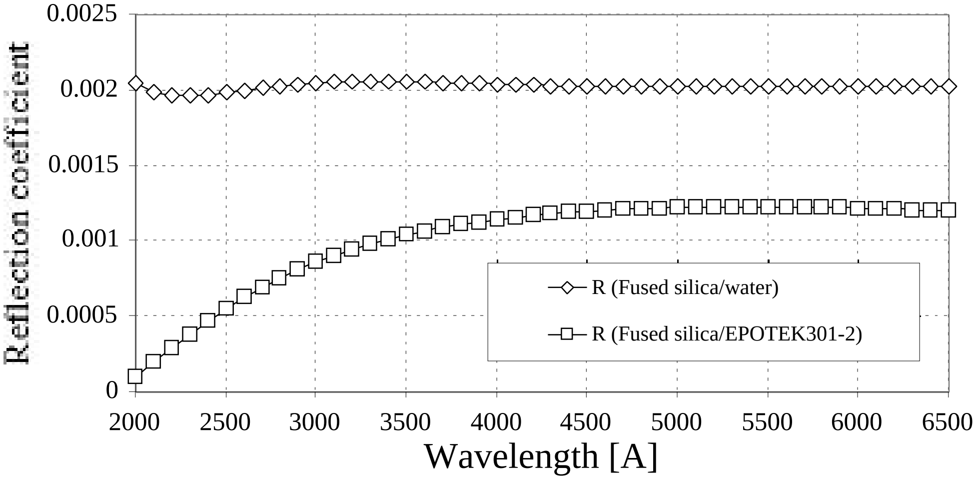

Figure 4. Wavelength dependence of the reflection coefficients for single fused silica-water, and fused silica-EPOTEK 301-2 interfaces at incidence angle of 0°. Notice that the fused silica-water reflection coefficient is almost independent of wavelength [5].

2.2. Optical Bandwidth of DIRC

Figure 5 shows a typical optical bandwidth of the DIRC detector for a particle at 90° polar angle in BaBar [5], taking into account the fact that half of the Cherenkov photons bounce forward, i.e., towards the mirror side, and half bounce backward, i.e., towards the wedges. The bandwidth is somewhat sensitive to the track dip angle. One can see that the bandwidth is cut at ~300nm, mainly due to the EPOTEK 301-2 glue transmission properties. This is actually advantageous for the DIRC because it reduces the chromatic error contributions to the overall Cherenkov angle and timing resolution. In addition, it makes the DIRC sensitive mainly in the visible wavelength region adding many practical advantages from a construction point of view.

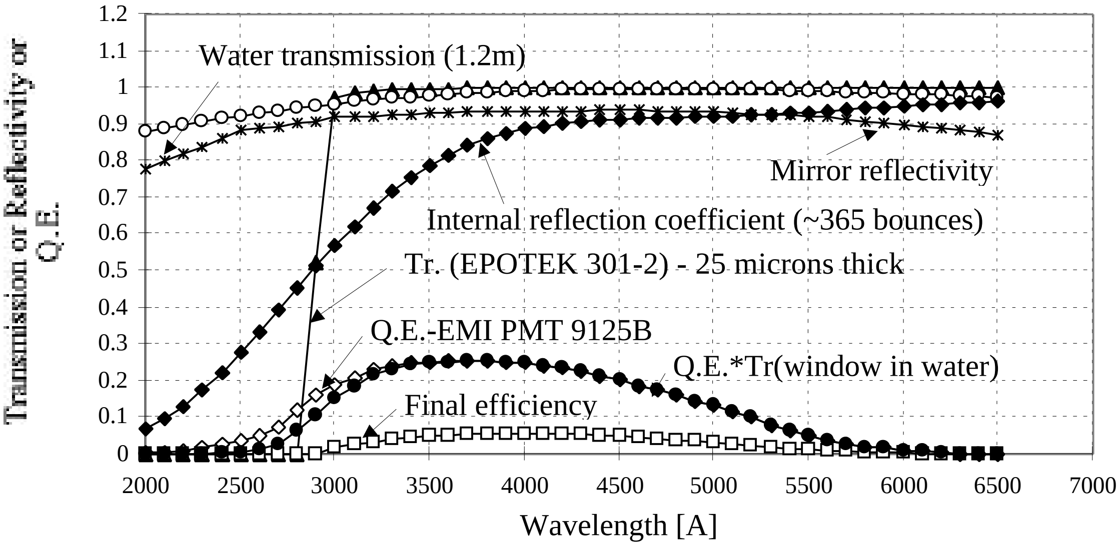

Figure 5. Contributions to the photoelectron detection efficiency for a track perpendicular to the fused silica bar located in the middle of the BaBar sensitive area, the quantum efficiency of the EMI9125B PMT is taken from manufacturer's data, a transmission of one glue joint (25 μm thick) made with EPOTEK 301-2 optical epoxy, water transmission over a 1.2 m long path, mirror reflectivity (affecting forward bouncing photons only), the internal reflection coefficient assuming ~365 bounces (averaging over forward and backward photons). The DIRC final efficiency takes into account many other correction factors as well [5].

2.3. Optical Homogeneity of Fused Silica Material

One of the least expected features of the synthetic fused silica material produced in long ingots, such as used for DIRC, was that it possesses an observable periodic optical non-homogeneity in its volume [6]. This effect was initially discovered while shining a laser beam at non-zero angles relative to the bar axis and observing that some light was scattered into a diffraction-like pattern, called "lobes" (see Fig.6). This effect was observed in both types of fused silica considered for use in the DIRC – Heraeus Suprasil[2] and QPC Spectrosil[3].

This "lobe effect" was taken very seriously because it could cause photon losses, or image distortion of the Cherenkov light. A few additional features of the lobe effect were immediately observed:

a) The lobes were produced over a range of incident angles typically less than 45 degrees (or greater than 135º) relative to the bar axis.

b) For a given bar that produced lobes for incident angles less than 90 degrees relative to the bar axis, no lobes would be observed for angles greater than 90 degrees, and vice-versa.

c) Some bars produced no lobes at all.

The lobe pattern was suggestive of diffraction off of a periodic structure in the fused silica [9]. In fact, such a pattern could be directly observed using ordinary white light either in a microscope or with the collimated light of a slide projector. Figure 7 shows the pattern observed with an optical digital microscope configured as shown in Fig. 8. The same "directionality" was observed as for lobe production - i.e. the pattern was observed for $\theta>0$, but not for $\theta<0$. Also, the pattern persisted after removing ~2mm of material from each surface of the bar, thereby establishing that the pattern is in the volume of the fused silica material.

---

[2] Synthetic fused silica material Suprasil Standard was made by Heraeus Amersil Co., 3473 Satelite Blvd., Duluth, GA 30136-5821.

[3] Synthetic fused silica Spectrosil 2000 "high OH". Spectrosil is a trademark of TSL Group PCL, Wallsend, Tyne on Wear, NE28 6DG, England; Sold in the USA by Quartz Products Co. (QPC), 160 W. Lee Street, Louisville, Kentucky 40201.

Although the lobe effect was initially observed in Heraeus fused silica, it is also present, although at lower intensity, in QPC fused silica material. Figure 9 shows the output of a photodiode as it is scanned across the lobe patterns of the two types of fused silica measuring the relative intensity. Evidently, the intensity of the lobes from QPC fused silica material (~$3x10^{-4}$) is much smaller than from Heraeus (~$3x10^{-2}$).

Figure 10 shows a model of the structure of the optical inhomogeneity, where it is assumed that there are curved "layers" of varying index of refraction within the fused silica ingots from which the bars are produced. If a laser beam is traveling tangent to these layers, than it would, in effect, see a "diffraction grating" formed by the alternating layers of high and low refraction index, thereby producing lobes. If however, the beam is traveling perpendicular to the layers, no lobes would be produced. This explains the "directionality" described above. Furthermore, we would expect that the opening angle of the lobes would be given by $\alpha = \lambda/\lambda'$, where λ is the wavelength of light and λ' is the spacing of the layers. Also, the phase change produced by the inhomogeneity would be $\Delta\phi = 4\,\pi\, a\, (R\, \lambda')^{1/2} / \lambda$, where a is the amplitude of the inhomogeneity and R is the radius of curvature of the layers, which we assume are circular. The power in the lobes is proportional to the square of the phase change. So $f \sim 1 / \lambda^2$. Measuring the lobes with two different light wavelengths can test the model. Figure 11 shows the results of the scans with HeCd blue line (442nm) and the HeNe red line (633nm). Table 1 shows the ratio of opening angles and lobe powers predicted by the model and those observed. The good agreement between the model and the measurements gives us confidence that the model is correct. Converting the measured power in the lobes to inhomogeneity amplitude (a), we find a = $6x10^{-6}$ for Heraeus and $1x10^{-6}$ for QPC. More detailed measurements can also measure the shape of the layers in the fused silica.

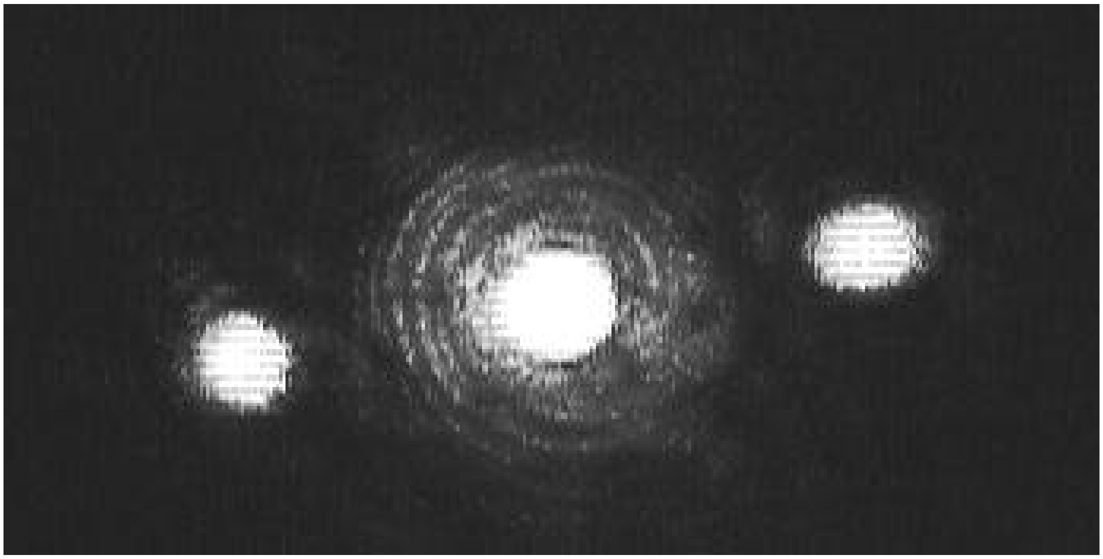

Figure 6. A lobe pattern created with a Ne-He laser in the synthetic fused silica Suprasil Standard [6].

Table 1 – Ratio of opening angles and power in the lobes.

Variable	Predicted	Measured
α (Blue) / α (red)	0.70	0.69 ± 0.03
f (blue) / f (red)	2.05	2.58 ± 0.40

Because of its bright lobes, Heraeus material was rejected for use in the DIRC. QPC fused silica was deemed acceptable because of its lower lobe power, which was about 100 times weaker than Heraeus. Also, the lobes in QPC fused silica were usually produced at angles close to perpendicular to the bar axis, which are not relevant for the DIRC. It is interesting to note that no such lobes have been observed in any of our samples of natural silica, nor in the synthetic fused silica windows used for the CRID TPC detectors and liquid radiators [7]. In all of these cases, the SiO2 material is randomly deposited on top of previous layers. What makes the DIRC's synthetic material so special is that it is produced in a long ingot form, where the $Si0_2$ material is deposited layer-by-layer while the ingot is rotating. The details of this process are proprietary, and so not directly accessible to us, but it seems very plausible that inhomogeneity amplitudes of a few times 10^{-6} could easily be produced by it. We should also point out that in most applications of synthetic fused silica, such as windows or optical fibers, the light is expected to travel only at angles close to parallel with the "bar axis". The DIRC may be one of the few applications where light must propagate at large angles with respect to this axis, and thus is sensitive to the "lobe effect".

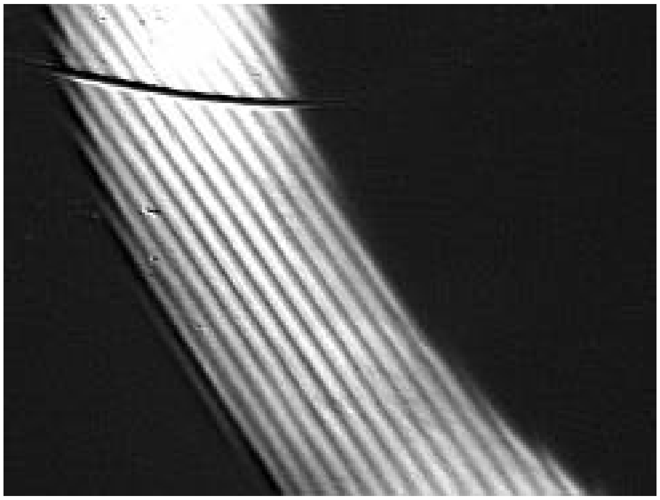

Figure 7. Image observed under a microscope using a “white” ring-type light. The periodic structure is evident. The dark line across the top is a100 μm wire placed on the top surface and used for scaling. The periodic structure was observed only at an specific angle, and only for the synthetic fused silica Suprasil Standard. No obvious periodic pattern was observed with the “high OH” Spectrosil 2000 [6].

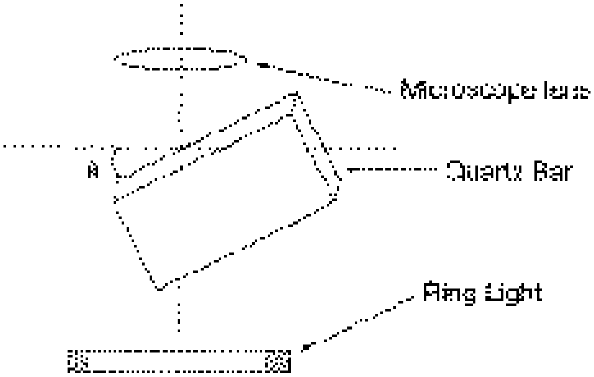

Figure 8. A microscope setup to observe the ring pattern as shown in Fig. 6 [6].

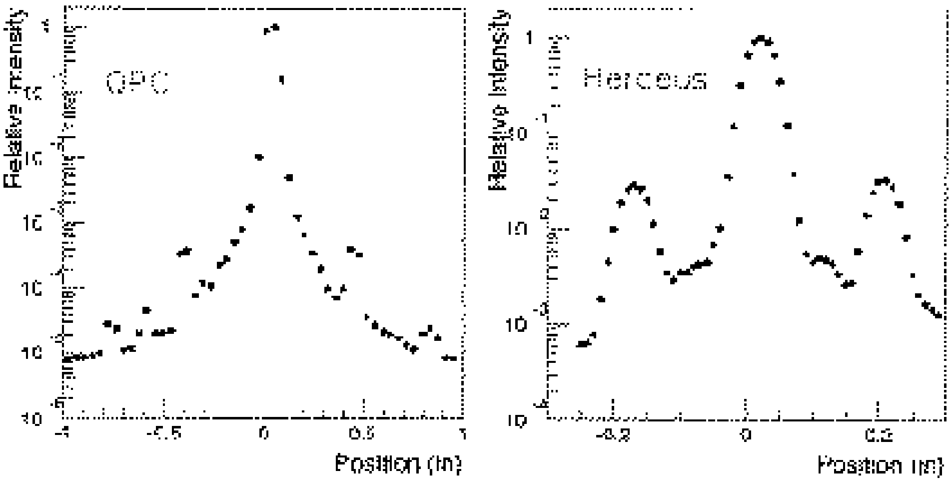

Figure 9 An interference pattern observed with a HeNe laser (633 nm) for QPC material (left) and Heraeus Spactrasil material (right). Note different scales [6].

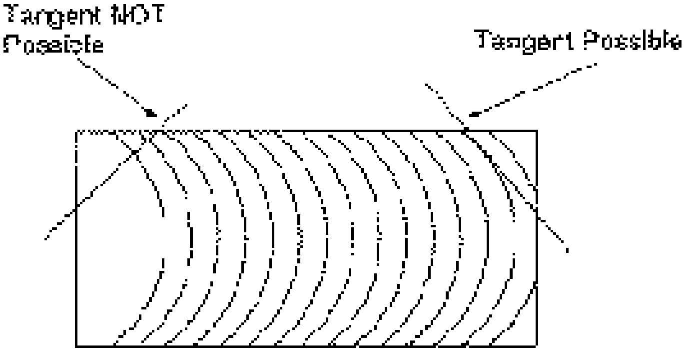

Figure 10. A possible explanation of origin of the interference is in the layering of the SiO_2 material within the ingot.

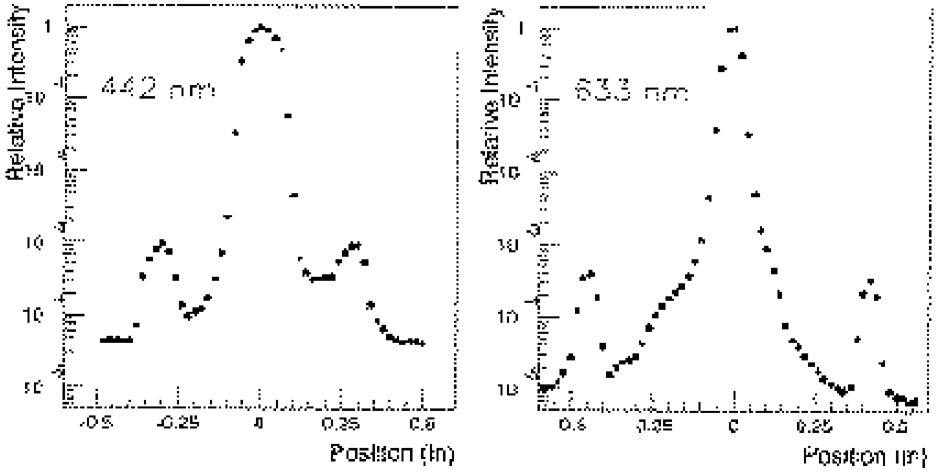

Figure 11. An interference pattern observed at two different wavelengths for the QPC material. The difference in the width of the peaks is due to the different spot size of the HeNe and HeCd laser beams [6].

A more challenging exercise is to explain the periodic pattern shown in Fig. 7, which was produced with a white ring light. A possible method to explain it is to assume that the periodic structure of the refraction index of the fused silica modulates the refraction angle of light rays as they enter the fused silica. In this model, we would not loose the light on average, there is just a periodic modulation of the light intensity. From the point of view of DIRC, we would not loose photons, we would affect their angular resolution. Although this explanation seems reasonable, it has not been directly proven experimentally.

Based on these tests, DIRC has chosen QPC Spectrosil 2000 as the material for bars.

3. FUSED SILICA BAR TRANSMISSION AND INTERNAL REFLECTION COEFFICIENT

Figure 12 shows a schematic of the setup that has been used to measure the bar transmission and relative internal reflection coefficient [10]. A He-Cd laser provides a vertically polarized laser beam with a wavelength of 442 or 325nm. The bar can be scanned through the laser beam using an actuator controlled by a Macintosh computer running LabView software program. The transmission was measured along the axis of the bar. The reflection coefficient was measured by allowing many bounces within the bar – see Fig. 13. The computer-controlled setup measured the relative internal reflection coefficient, which could be normalized by comparison with a reference bar whose absolute reflection coefficient was measured by the method described in the next chapter. The laser beam enters the bar at the Brewster angle (see Fig. 12), which simplifies the overall problem by allowing the measurement of only two intensities rather than four required in the absolute measurement. The advantage of the automatic method is that it scanned about 75 grid-points across a large surface area. A number of bars have been tested in this setup. The average relative internal reflection coefficient was 0.9996±0.0001, the average transmission was 99.9±0.1%/meter at 442nm, and 98.9±0.2% at 325nm. Figure 14 shows an example of measurement results at 442nm [11].

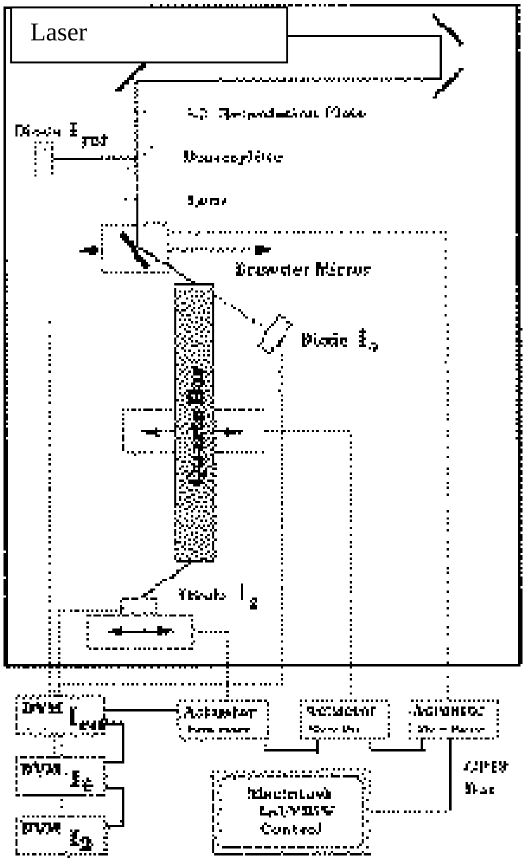

Figure 12. Computer controlled setup used to measure fused silica bar transmissions and the relative internal reflection coefficient [10].

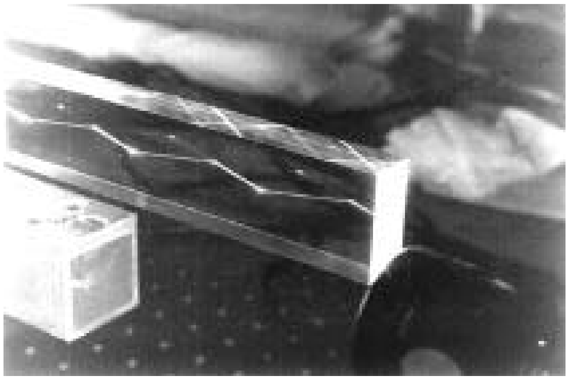

Figure 13. A laser beam bouncing in the fused silica bar during the relative internal reflection coefficient measurement [10].

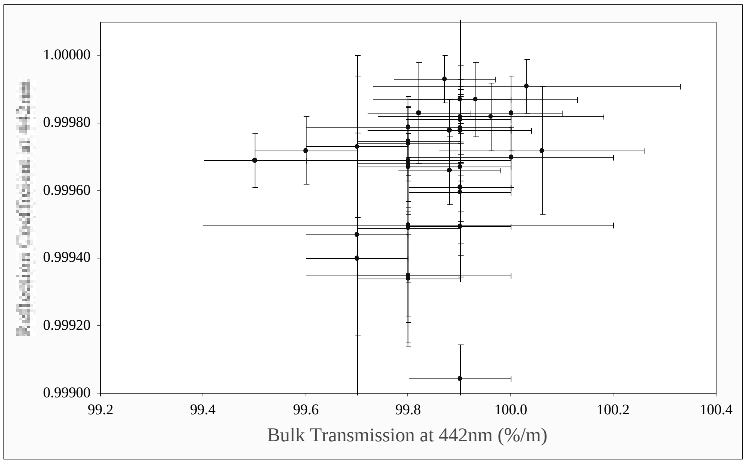

Figure 14. Measurements of transmission and relative internal reflection coefficient at a wavelength of 442nm [11].

4. FUSED SILICA BAR INTERNAL REFLECTION COEFFICIENT AS A FUNCTION OF WAVELENGTH AND SURFACE POLLUTION

The fused silica bar used in this measurement is 1.2247 m long, 3.495 cm wide and 1.646 cm thick. The internal reflection coefficient was measured on the wide surfaces of the bar [5]. Prior to this measurement, the bar surfaces were cleaned using an alumina powder technique. This is done by gently rubbing the fused silica surface with 0.3µm alumina powder, which is mixed with clean water in a 1:10 ratio, ensuring that the surface chemical pollution was minimized. Cleaning was essential for optimum results. A randomly picked bar, which was not subjected to either the “alumina powder” cleaning or the regular “acetone/alcohol” DIRC cleaning procedures, could have a reflection coefficient lower by ~0.0005. During the DIRC construction, we carefully monitored the bar cleanliness using the relative measurements of the reflection coefficient [11,12] normalized to carefully selected reference bars.

To measure the wavelength dependency, we used five laser wavelengths: 266, 325, 442, 543, and 633nm, which were provided by four different lasers: Nanolase solid state YAG laser (266nm), Lyconix He-Cd 4210N (325 or 442nm), Uniphase 1135 green (543nm), and Uniphase red (633nm). The intensity of the lasers was different, influencing the relative accuracy for each measurement (for example, the Hamamatsu photodiode currents were ~500-600µA at 442nm, ~20-25µA at 325nm, ~10-15µA at 266nm, ~20-25µA at 543nm, and ~500-550µA at 633nm). Similarly, laser stability varied, with the 266nm Nanolase being the least stable one.

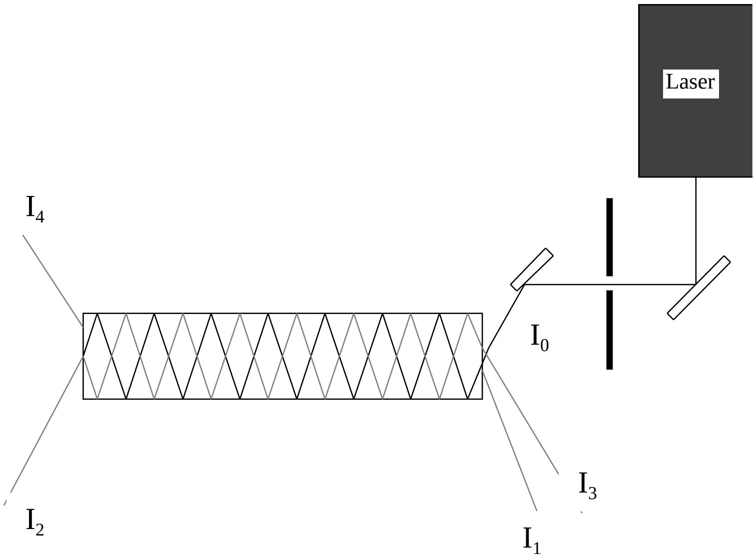

Figure 15. A schematic layout of the experiment to measure the reflection coefficient.

One could adopt a complicated method to measure the internal reflection coefficient, which assumes a complete optical analysis, including measurements of the entrance and exit angles. However, we have invented a simpler method, called the "calorimetric" method [13]. This method simply measures five light intensities (see Fig. 15), the number of light bounces, and also uses bar dimensions, i.e., no entrance or exit laser light angles are present in the measurement. The measurement was made by hand with a single photodiode measuring all intensities. The photodiode was equipped with a diffuser to improve its non-uniform response; however, it was still necessary to peak the diode by hand to achieve the reproducible results. We used the second photodiode to monitor the laser intensity. Both photodiodes were synchronized during the readout. The internal reflection coefficient [r] is measured absolutely with this technique. The starting equation is:

$$(((I_0 - I_1)\,r^N - I_2)\,r^N - I_3)\,r^N = I_4 \tag{1}$$

which in turn leads to

$$I_0 = I_1 + I_2\,x + I_3\,x^2 + I_4\,x^3 \tag{2}$$

The solution X is related to the coefficient of internal reflection [r] through the following equation:

$$\begin{aligned} x^{-1} &= r^N * \exp\{-\frac{L}{\Lambda} * \sqrt{[1+(\frac{bN}{L})^2]}\}\,, \\ &= (\mathrm{Reflection\_coeff.})^N * \mathrm{Transmission\_coeff}, \end{aligned} \tag{3}$$

where N is the number of bounces, L is the length of the fused silica bar, b is the width of the fused silica bar, Λ is the fused silica attenuation length, and I_i the laser intensities. The laser setup was arranged to have N = 54 bounces at 442nm. The fused silica attenuation length Λ is not an easy quantity to measure at long wavelengths using such a short bar. We decided to use the attenuation length of Λ = 499.5±167 m at 442nm as a reference, and then scale it to any other wavelength λ according to $1/\lambda^4$, assuming Rayleigh's law. For example, this dependence gives Λ ~2100 m at 633nm, which would be impossible to measure with good accuracy using a ~1.2 m long bar.

A further improvement in accuracy is found, by adding another term in equation (2), which can be calculated from the measured intensities by integrating the infinite sum of higher order contributions:

$$I_0 = I_1 + I_2\ x + I_3\ x^2 + I_4\ x^3 + I_5 \qquad (4)$$

where the correction term reduces to:

$$I_5 = \frac{I_3^{\ 3}}{I_2\ (I_2 - I_3)} \qquad (5)$$

This correction increased the coefficient typically by ~0.0003.

Another small improvement in the accuracy was a correction for photodiode response due to the finite size of the laser beam. As the beam size for each intensity I_i changes, the correction is different for each I_i component. These corrections vary from 1.006 (I_0) to 1.03 (I_4).

The measurement of the reflection coefficient may be influenced by a loss of light intensity due to the interference effect described in the previous chapter. This effect could occur at some laser angle orientations relative to the bar axis. We made sure that the escaping laser beams do not have small lobes. In addition, one does not expect a large effect for this type of fused silica.

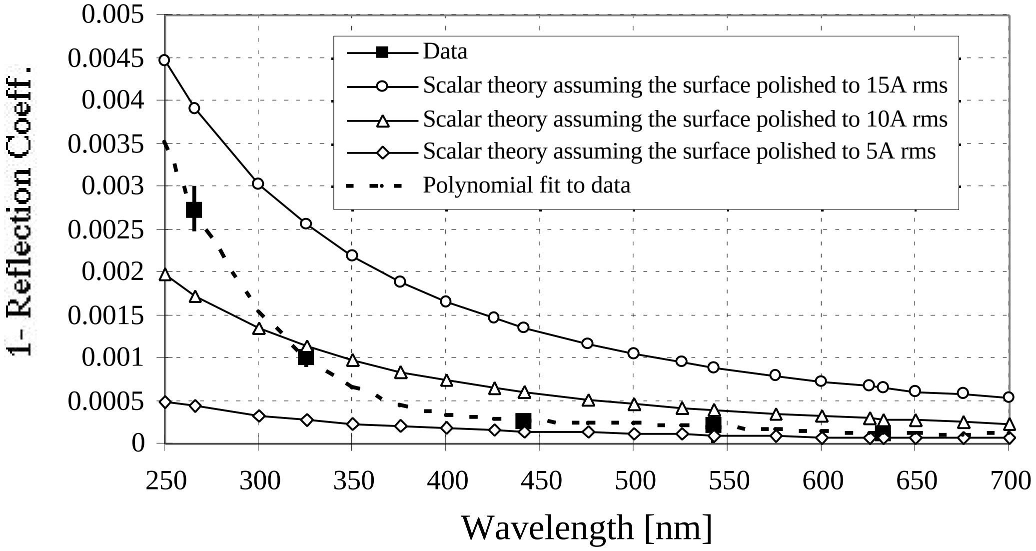

Figure 16. A comparison of the internal reflection coefficient measurements at five different laser wavelengths and the scalar scattering theory, assuming only random surface imperfections. Data are consistent with ~5-8 Å rms surface finish for wavelengths between 400 and 700nm. Below ~350nm, the data does not agree with the simple scattering theory. The laser light bounced from the wide sides of the bar [5]. The graph shows also a polynomial fit to data.

Figure 16 shows the final data, plotted as (1-Reflection coefficient) = f (wavelength). The plotted errors are based on the rms of ten repetitive trials for each intensity component I_i. The systematic errors are harder to evaluate. They depend on many factors, such as surface quality variation, surface pollution (especially in the far UV region), method of the photodiode "peaking" (i.e., finding a spot yielding a consistent maximum reading), dust, background light in the room, lobe effect due to the refraction index variation, etc. To evaluate at least some systematic errors, the measurements were repeated many times, while varying the laser entrance point into the bar, the laser path within the bar, the number of bounces N (by a few), avoiding bright spots observed when hitting either chips or the bar supporting buttons, etc. After a lot of practice, one can assign a systematic error of about ±0.0003 to each measurement. Figure 16 also shows three curves based on the scalar reflection theory [14], assuming the fused silica surface finish of 5, 10, and 15 Å. The internal reflection coefficient is consistent with the surface finish between 5 and 8 Å in the wavelength region between 450 and 650 nm. However, it gets significantly smaller below 350nm, and its value is no longer consistent with the scalar theory. This discrepancy is not well understood, although a considerable amount of time has been spent checking the experimental results at 266 and 325nm. A possible explanation for the discrepancy in the UV region could be a chemical pollution, or near surface humidity. Figure 16 also shows a polynomial fit to data. This fit was used to evaluate the DIRC efficiency and mean wavelength response [5].

We also did extensive pollution tests to see if the internal reflection coefficient can be degraded by materials used for the construction of the bar boxes, gluing or during general handling procedures. The work, as well as a list of materials used in the tests, is presented in Ref. 15. The tests were performed for extended periods of time at room and elevated temperatures with and without added humidity. None of the materials, summarized in Table 2, caused any significant decrease of the internal reflection coefficient at a level of about 0.0003.

Table 2. Summary of the tests of pollution candidates [15].

Pollution candidate	**Test duration [days]**	**Temperature**	**Humidity**	**Relevance to DIRC**
Gluing station	2	room	dry	Exposure to glue fumes during bar gluing
DP-190 epoxy (translucent)	31	room	dry	Used as secondary glue to seal bar boxes
DP-190 epoxy (gray)	31	room	dry	Used during construction of bar boxes
Wet Hysol 1C-LV epoxy	42	room	dry	Used as primary glue to seal bar boxes
Wet SES-403 RTV	54	room	dry	Not used in DIRC
Cured SES-403 RTV	74	room	dry	Not used in DIRC
Packing foam for bars	74	room	dry	Used to ship bars from Boeing Co. to SLAC.
EPDM gasket	74	room	dry	Used in gaskets for water seal
DIRC gas system at BaBar	90	room	dry	Final check of BaBAr tubing cleanliness
Wet Dow Corning 3145 RTV	116	room	dry	Used during the construction of the clean room
Teflon sample	116	room	dry	Not used in DIRC
Prototype bar box	117	room / 60ºC	dry	Initial test of bar box cleanliness
Epotek 301-2 epoxy	1	room	dry	Used to glue bars, wedges and windows
Bar box buttons	3	room	dry	Used in bar box construction
Matheson pressure regulator	10	room / 60ºC	dry / wet	Used in BaBar gas system
Magnehelic pressure gauge	31	room / 60ºC	dry / wet	Used in BaBar gas system
Disogrin O-rings	75	room / 60ºC	dry / wet	Used in BaBar gas system

5. RADIATION DAMAGE OF FUSED SILICA AND OPTICAL GLUES

It is expected that the DIRC could get 0.5-1 krad/year during its normal operation in 10 years. Of course, nobody can safely estimate a dose during the machine physics tuning, but it seems reasonable to insist that the the Cherenkov radiator is resistant up to at least 10-15 krad level.

For the initial DIRC prototype tests [16,17] we used Vitrosil-F[4], which is a natural fused silica material (from now on we call it “natural fused quartz”). Because of good results with it, based on optical performance, it was assumed that the BaBar DIRC would also use natural fused quartz. Radiation damage of the natural fused quartz was not expected in the early days of the DIRC proposal, at least at a dose level of 10-20 krads obtained

---

[4] Natural fused quartz material Vitrosil-F was made by Thermo-Syndicate Co.

from photons with energy of few MeV. Therefore, it was rather surprising to find that the Vitrosil-F material lost ~80% of transmission per meter at 325nm after a radiation dose of only ~7 krads [13] (see Fig. 17). The DIRC physics prototype tests were done with this type of natural fused quartz. After the radiation damage problem was realized, we decided to test two other natural fused quartz materials, namely, JGS3-IR[5] and T-08[6]. We obtained equally bad results. In principle, one could partially recover the transmission using photo-bleaching[7] (see Fig. 17), and/or a heat treatment[8] at 442nm and partially at 325nm. Such a "curing procedure" would be highly impractical to implement in BaBar. Therefore, it was decided not to use natural fused quartz, and instead, we switched to more expensive synthetic materials. To remind the reader, natural fused quartz is made out of crystalline quartz raw materials found in mines. Synthetic fused silica is made artificially out of a silicon tetra-chloride, or other feedstock.

We have conducted two types of tests: (a) using short quartz samples (~10-20 cm), where the transmission was measured typically with a monochromator, and (b) using long samples (~1 m), where the transmission was measured with a He-Cd laser (LiCONix 200 series; model 4214NB).

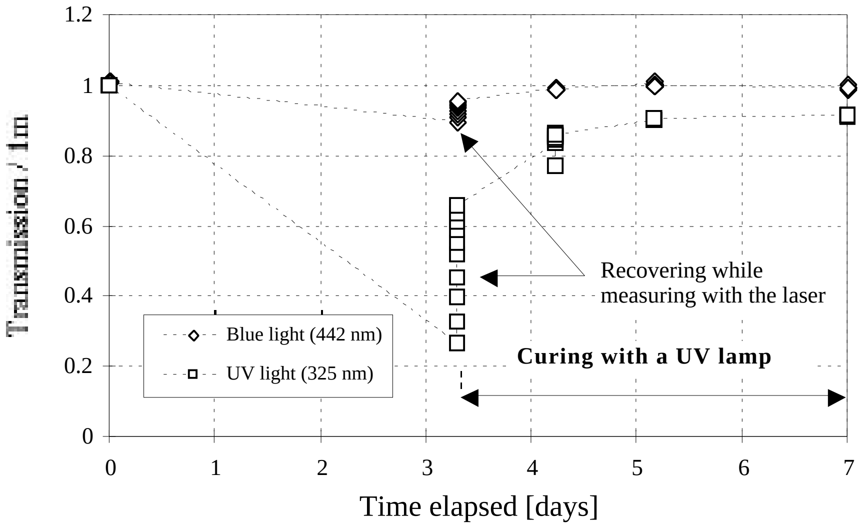

Figure 17. Radiation damage after radiation dose of ~7 krads, of natural fused quartz Vitrosil-F, made by Thermo-Syndicate Co. The relative measurement (corrected for the reference bar) was done with a laser at 325 and 442 nm wavelengths. The sample length was only ~30 cm, and the result was extrapolated to 1 m length. The radiation damage was partially removed by a strong UV lamp. Furthermore, can also see a larger recovery for each laser measurement. The recovery induced by the laser affected only a region close the laser beam's spatial extent [13].

5.1. Study of Radiation Damage of Short Samples of Synthetic Fused Silica

We used the Co^{60} source facility available at SLAC to perform these tests [13,19]. Its present activity is about 14.1 Curie. A short sample can be placed very close to the source and one can achieve a dose up to ~50-60 krads per day. The Co^{60} source gives two major photon emission lines, 1.173 and 1.333 MeV. There are some Compton electrons coming from the well concrete walls; we measured that they contribute about 10% to the total dose. The radiation dose was estimated using TLD dosimeters. The measurement was calibrated using (a) a theoretical estimate based on the geometry and known source activity corrected for its lifetime, (b) an ion chamber measurement, and (c) an opti-chromic dosimeter measurement. The measurements agreed to within ~10%.

---

[5] Natural fused quartz material JGS3-IR was made by the Institute of Technology, Beijing 100081, P.R. China.

[6] Natural fused quartz material T-08 was made by Heraeus-Amersil Co.

[7] Photo bleaching is a recovery of lost transmission due to the radiation damage by a high intensity UV laser or lamp [18].

[8] A heat treatment can also recover the transmission loss due to the radiation damage.

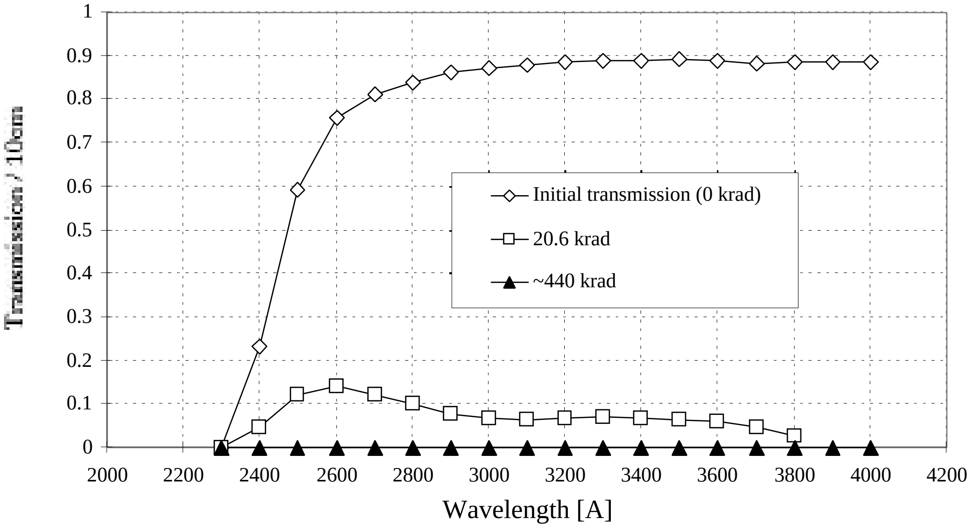

Figure 18. Radiation damage of natural fused quartz JGS3-IR sample. After a dose of ~440 krads, the sample became almost black. Not corrected for the Fresnel reflection [13].

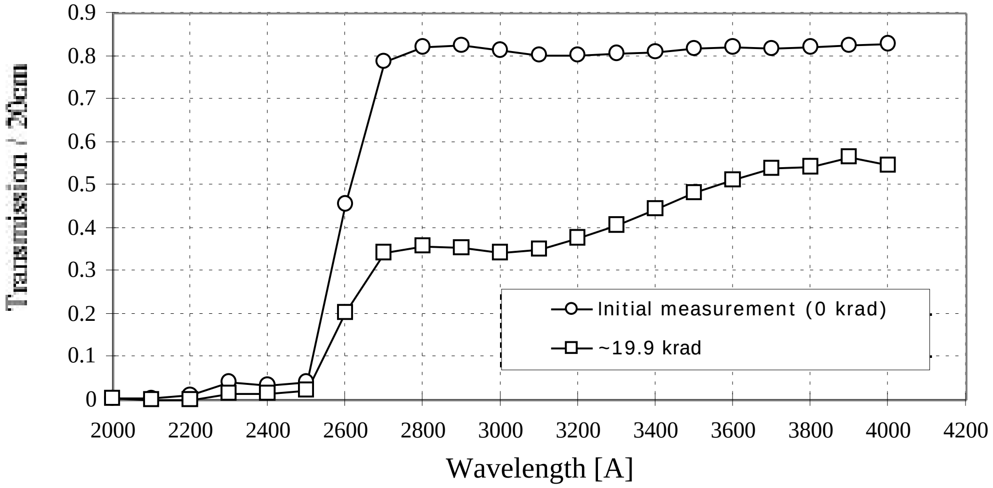

Figure 19. Radiation damage of natural fused quartz T-08 from Heraeus. Not corrected for the Fresnel reflection [13].

The transmission measurements of the short samples were typically done using the monochromator. These measurements have systematic errors at a level of 1%. Figures 18 and 19 show examples of such measurements for the natural fused quartz samples. One can see a serious loss of transmission after a dose of only 20 krads. DIRC with the 5-meter long bars would not function at all given such transmission.

It was noticed that all three natural fused quartz samples differ from each other in their radiation response. Some differences were easily noticed during visual inspection. For example, the Vitrosil F samples remained perfectly clear to the naked eye even after ~100 krad (although its transmission was actually damaged, as discussed above). The JGS3-IR sample developed a uniform coffee-brown color after ~20 krad, and became almost black after ~440 krad. On the other hand, the T-08 sample was perfectly clear after ~10 krad, and only slightly yellow after ~334 krad, when inspected visually. However, we discovered that the monochromator PMT's single rates increased by a factor of ~37 after a dose of ~10 krads, and by a factor of ~8500 after a dose of ~334 krads (the rate was approaching ~450 kHz). We believe that the rate increase after the irradiation was caused by a very strong radio-luminescence [20] of natural fused quartz initiated by the Co^{60} radiation. Both Vitrosil-F and JGS3-IR samples did not show any noticeable radio-luminescence after the irradiation, at least at room temperature. The effect was not tested at elevated temperatures. We were not equipped to test very short radio-luminescence time constants. The first measurements were usually done within 30-60 minutes after the sample was removed from the radiation well.

It is clear that natural fused quartz is not a good candidate for the BaBar experiment, and therefore, we began to study the properties of synthetic fused silica material. We have tested four short synthetic fused silica samples, (a) JGS1-UV[9] 2 cm x 2 cm x 10 cm sample, (b) Suprasil Standard 2 cm dia. x 20 cm long sample, (c) "high OH" Spectrosil 2000 (~1000 ppm OH content) 2 cm x 2 cm x 20.7 cm long sample, and (d) "high OH" Spectrosil B[10] 2 cm dia. x 20 cm long sample. Figures 20-24 show the results of this study.

Figure 20 shows transmission levels for several doses of the "high OH" Spectrosil B 20 cm long sample. We find that the material is radiation hard above 280nm. In the far UV region below 240nm, we observe some radiation sensitivity. However it is still within acceptable levels for the BaBar experiment. This sample showed a strong radio-luminescence after radiation exposure, as one can see in Fig. 21. The photonic activity was estimated with the monochromator's PMT, and was about 100 times more than normal after ~12 krads, and was decaying at a rate of about 10% after 2-3 minutes. The time interval between the end of the irradiation and the beginning of the transmission measurement was typically 30-40 minutes.

Figure 22 shows that JGS1-UV synthetic material is very radiation resistant. In fact, it is among best samples we have tested. This sample did not show any radio-luminescence after radiation exposure.

Figure 23 shows that the Suprasil Standard synthetic material showed the largest radiation damage for all synthetic materials we have tested so far. We find that the material is radiation hard for small doses up to 10-20 krads. However, when the dose was increased to ~280 krads, we see a substantial transmission loss below ~340nm. Furthermore, this particular material did show a strong radio-luminescence after radiation exposure.

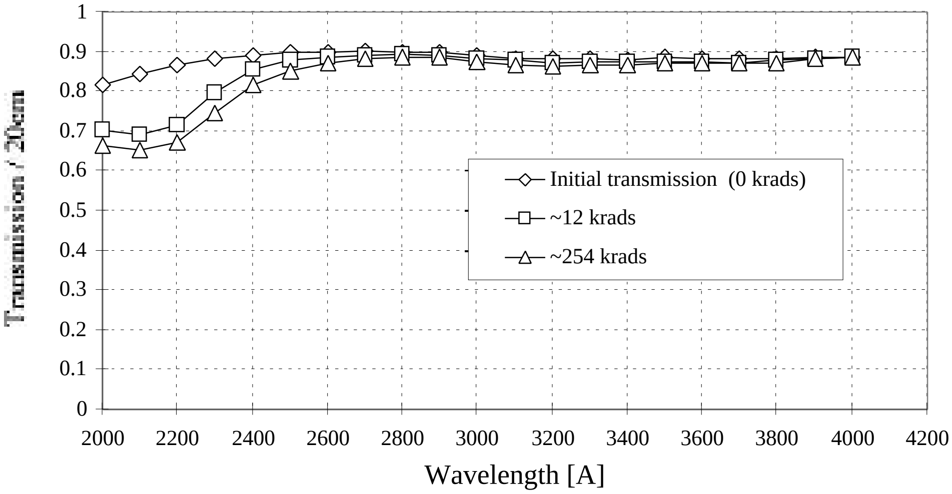

Figure 20. Radiation damage of the synthetic fused silica "high OH" Spectrosil B, made by QPC Co.. Not corrected for the Fresnel reflection [19].

---

[9] Synthetic fused silica material JGS1-UV was made by the Institute of Technology, Beijing 100081, P.R. China.

[10] Synthetic fused silica material Spectrosil B "high OH" was also made also by TSL and sold by QPC.

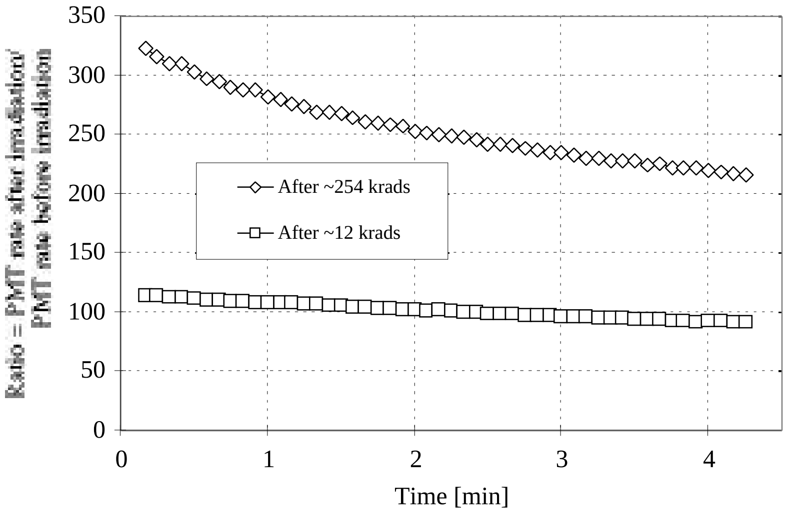

Figure 21. Radio luminescence of the synthetic fused silica "high OH" Spectrosil B, as seen by two PMTs in the monochromator [19]. The measurement was done half an hour after removing the sample from the Co^{60} well.

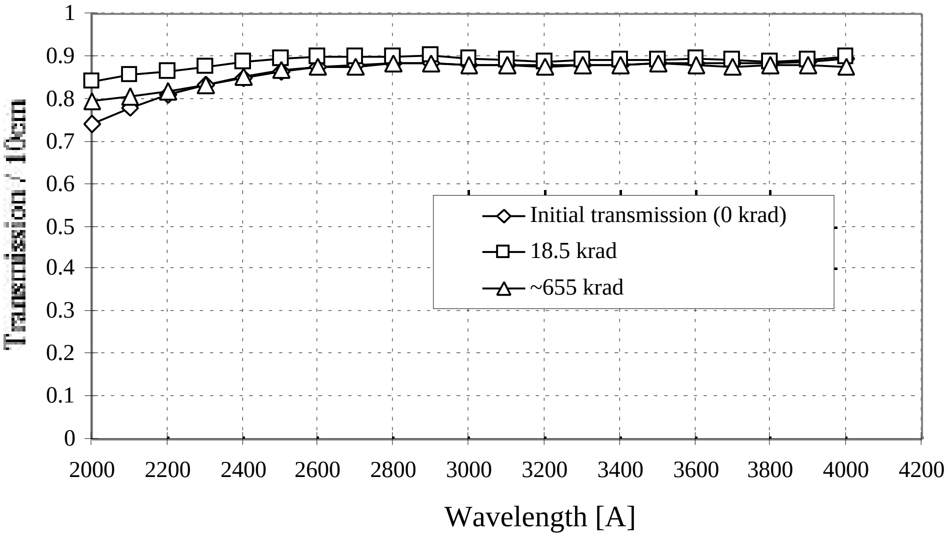

Figure 22. Radiation damage of the synthetic fused silica JGS1-UV sample. Not corrected for the Fresnel reflection [19].

Figure 24 shows transmission for several irradiation doses of the "high OH" Spectrosil 2000 20.7 cm long sample. This particular synthetic material shows a good radiation resistivity. We find that the material lost 2-3 ± (1-2) %/meter of transmission above 260 nm after a dose of ~17 krads. In the far UV region below 240 nm, we observe larger losses. However, it continues to be well within the BaBar specs. This sample did not show any radio-luminescence after radiation exposure. Table 3 summarizes all radiation damage tests with all types of quartz.

The subject of radiation damage is complicated. The radiation damage is caused generally by quartz defects, such as oxygen vacancies, impurities (Ge, Ti, Al, alkali ions, OH), etc. [20]. The defects can act as the color centers or become sources of radio-luminescence. The radio-luminescence is a well-known photon emission effect in quartz as well as in other materials. This technique has been used to date ancient pottery, because it always contained some quartz impurities (a sample of quartz is subjected to a temperature sweep and the resulting photon activity is measured with a PMT). One can identify the origins of different species of quartz. Not only can one identify a specific quartz defect from a given peak position in the radio-luminescent spectrum, but for the same quartz materials, such as the natural pink quartz, radio-luminescence begins at room temperature. Some materials have to be heated to more than 100^{o}C. Radio-luminescence occurs also in synthetic fused silica materials at some level.

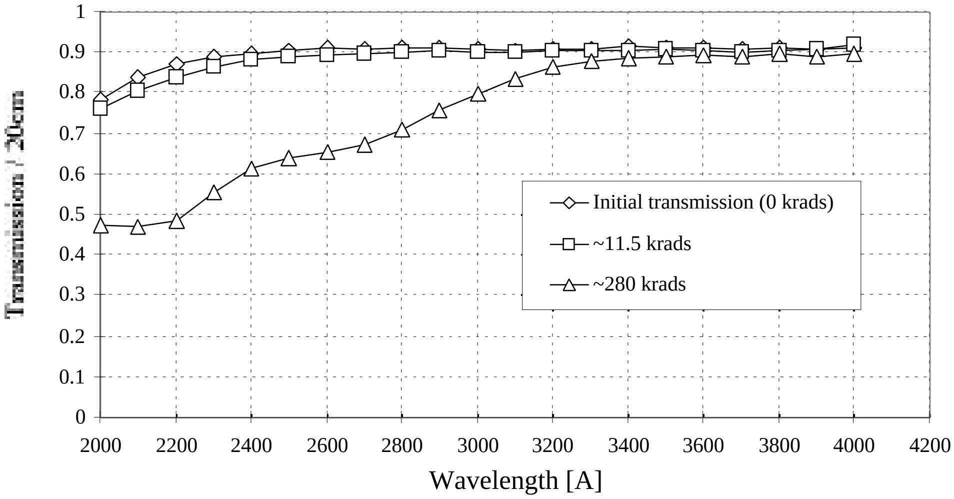

Figure 23. Radiation damage of the synthetic fused silica Suprasil Standard from Heraeus sample. Not corrected for the Fresnel reflection [19].

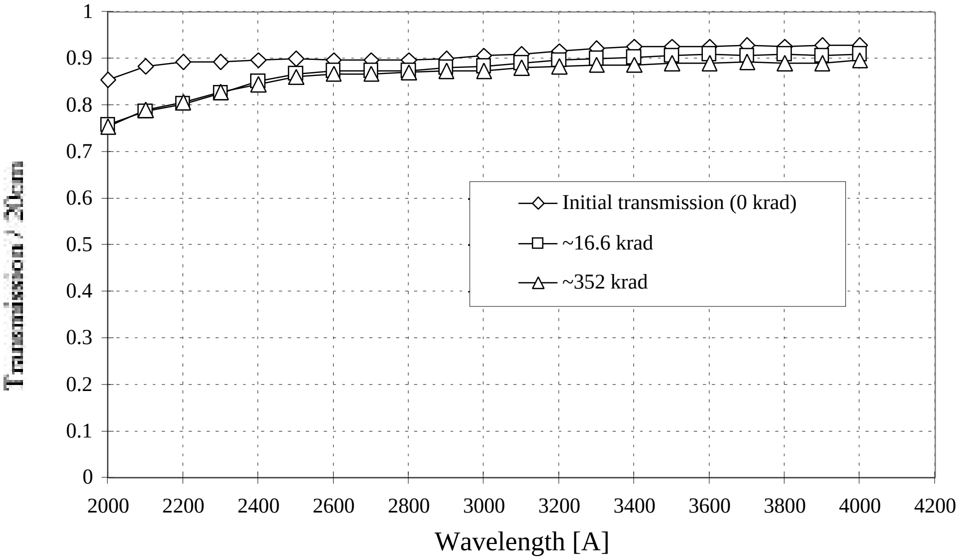

Figure 24. Radiation damage of the synthetic fused silica "high OH" Spectrosil 2000 sample. Not corrected for the Fresnel reflection [19].

Table 3. Radiation damage for various types of short natural and synthetic fused quartz samples [13,19].

Quartz material	Source	Type of quartz	Special comment	Visual change	Radio luminescence	Transmission loss
Vitrosil F	TSL	Natural	DIRC prototypes	No (after ~100 krad)	No (after ~100 krad)	Severe (after ~7 krad)
T-08	Heraeus Amersil	Natural		Slight yellow (after ~330 krad)	Yes (after ~330 krad)	Severe (after ~10 krad)
JGS3-IR	Beijing Institute	Natural		Dark brown (after ~400 krad)	No (after ~400 krad)	Severe (after ~20 krad)
Suprasil Standard	Heraeus Amersil	Synthetic		No (after ~280 krad)	Yes (after ~280 krad)	Small (after ~280 krad)
JGS1-UV	Beijing Institute	Synthetic		No (after ~650 krad)	No (after ~650 krad)	No (after ~650 krad)
Spectrosil 2000, “high OH”	TSL	Synthetic	Used in final DIRC	No (after ~180 krad)	No (after ~180 krad)	Small (after ~180 krad)
Spectrosil B “high OH”	TSL	Synthetic		No (after ~254 krad)	Yes (after ~254 krad)	Small (after ~254 krad)

5.2. Study of Radiation Damage of Long Synthetic Fused Silica Samples

The transmission measurements of the long fused silica samples were done using the laser scanning system developed by the DIRC group [12] and described in chapter 3. This setup is capable of measuring the average transmission within a systematic error of about 0.2%.

We have tested two synthetic fused silica materials: (a) a Suprasil Standard rod, 100 cm long and 26 mm in diameter, and (b) a “high OH” Spectrosil 2000 rod, 137 cm long and 55 mm diameter [19].

The long fused silica samples are irradiated using a Co^{60} source at LBL. Its activity is ~1400 Curie. At a distance of 1 meter from the source, one can achieve a dose of ~38 kR per day. The bar is placed perpendicular to the geometric axis of the source. The radiation dose was measured with a Victoreen dosimeter measuring the exposure (in roentgen units [R], 1 R = 2.58 10^{-4} Coul kg^{-1}). The TLD dosimeter measures the absorbed dose (in rad units, 1 rad = 1.139 R in tissue, it depends on the material and can change). In the following, the radiation doses will be given in terms of exposure dose, using roentgen (R) units.

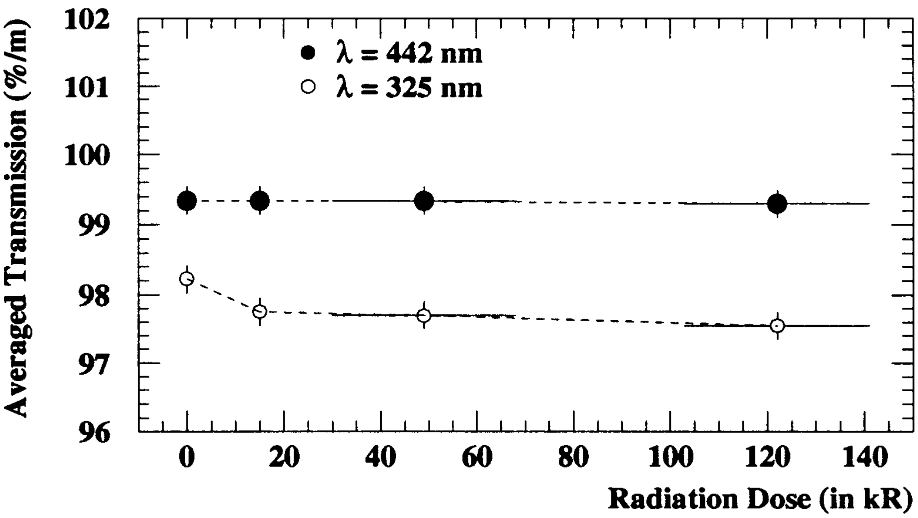

Figure 25. Radiation damage of the synthetic fused silica “high OH” Spectrosil 2000 (137 cm long) sample. This measurement was corrected for the Fresnel reflection at two surfaces. [19]

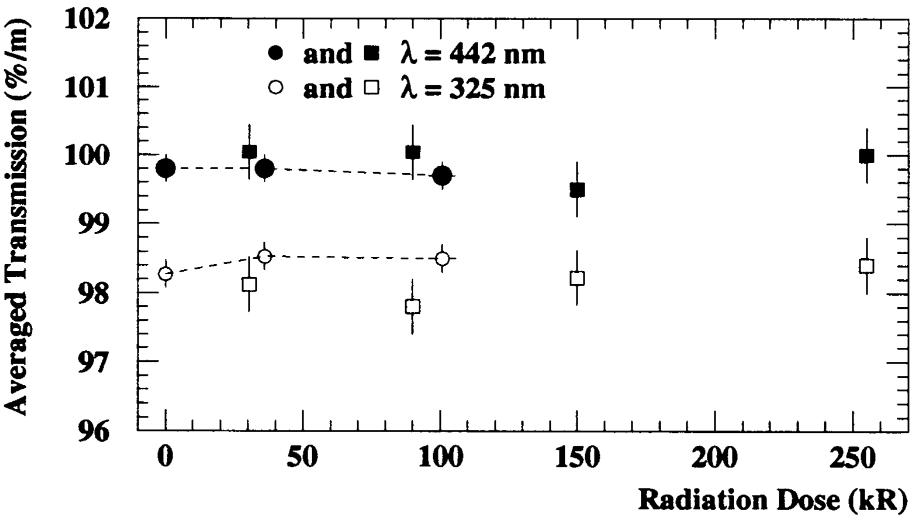

Figure 26. Radiation damage of the synthetic fused silica Suprasil Standard (100 cm long) sample. This measurement was corrected for the Fresnel reflection at two surfaces [19].

Figure 25 shows the transmission measurements for Spectrosil 2000. We find that the material lost ~0.5% of transmission at 325nm after 15 kR. Increasing the dose further did not result in additional transmission loss. No effect was observed at 442nm for all radiation doses. Figure 26 shows the transmission measurements for Suprasil Standard. No significant transmission loss was observed at 325nm or 442nm. This result is consistent with the radiation damage observed in the small samples, but does not extend into the UV.

Based on the radiation test results, we have found that the QPC Spectrosil 2000 fused silica material satisfies requirements for the radiation hardness needed to operate successfully for 10 years at BaBar.

5.3. Study of Radiation Damage in Optical Glues

It was also important to test the radiation hardness of the optical glues, which could fail either due to radiation or background induced photonic activity in the bar. We have tested five glue candidates: (a) EPOTEK 301-2 optical epoxy (it was the glue actually used for gluing of all DIRC fused silica bars), (b) SES-403 RTV, (c) SES-406 RTV, (d) KE-108 RTV,[11] and (e) Rhodorsil-141 RTV.[12] All optical glue samples were tested using the SLAC Co^{60} source facility. The following procedure was used: a glue sample was placed between two small fused silica windows, each 4mm thick. This particular fused silica window was tested to be radiation resistant up to at least 70 krads, or more, but we did not test it further. It cuts the transparency at around 170nm, i.e., it does not influence the glue studies in this note. The glue samples were placed in the monochromator to check the initial transmission, then irradiated with a dose of about 60-70 krads, and then rechecked for transmission.

Figure 27 shows the overall transmission summary and the experimental setup used in measurements. Figure 28 shows the transmission for the EPOTEK 301-2 epoxy, which is an optical epoxy with a UV cut-off edge at ~280nm. One can see a slight damage of the transmission at a 1% level, between 300 and 350nm, after a dose of ~70 krads. The thickness of the EPOTEK sample was ~25μm. This thickness is typically used for gluing bars together.

---

[11] Optical RTV glues SES-403 RTV, SES-406 RTV, and KE-108 RTV are made by Shin-Etsu Co..

[12] Optical RTV glue Rhodorsil-141 RTV was made by Rhone-Poulenc Co..

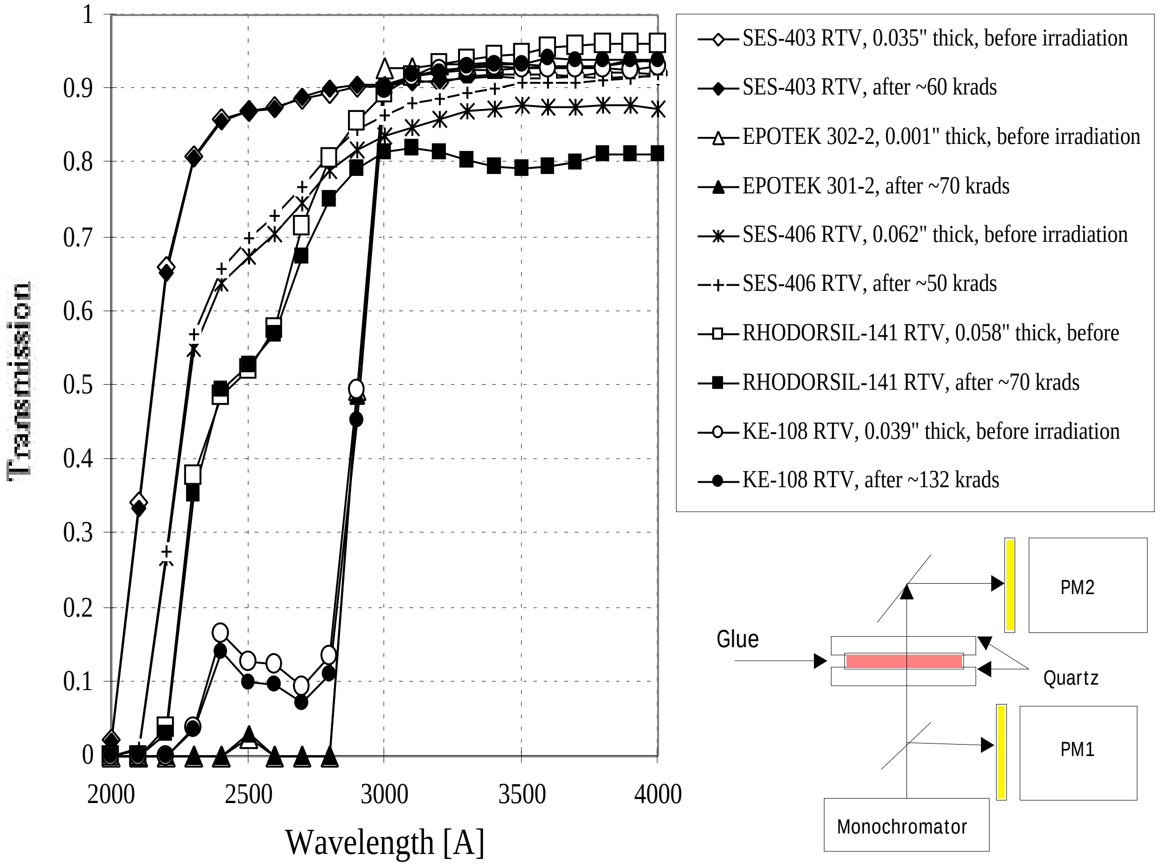

Figure 27. Radiation damage of various DIRC optical glue candidates with Co^{60} source.. The glue was placed between two fused silica plates, which were radiation hard. The glue sample was typically ~25 μm thick [19].

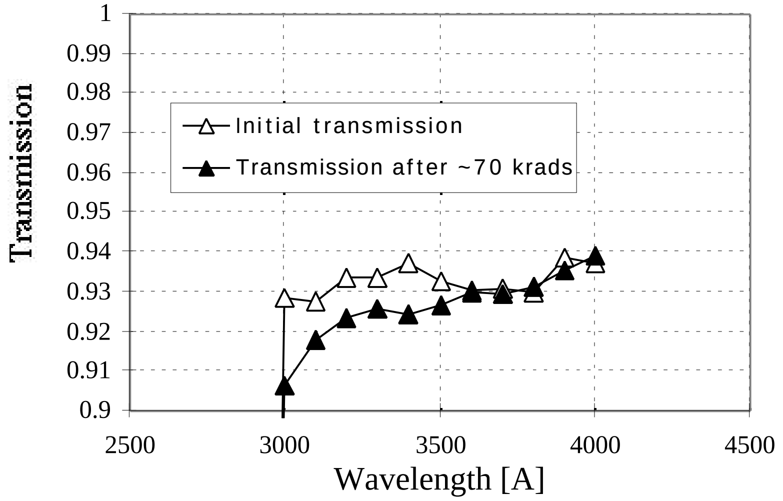

Figure 28. Radiation damage of the optical epoxy EPOTEK-301-2, which was used to glue together DIRC bars. The glue sample was ~25 μm thick, which is similar to a typical thickness for gluing bars together. This measurement was corrected for the Fresnel reflection at two surfaces [19].

Based on the radiation test results, we have found that the EPOTEK-301-2 epoxy, which was chosen to glue the bars together, also satisfies requirements for the radiation hardness needed to operate successfully for 10 years at BaBar. In addition, we have not observed any “yellowing” effects of this glue under a strong flux of photons.

6. REFLECTION FROM THE FUSED SILICA BAR SUPPORTING SHIMS AND MIRRORS

The mirror[13] at the end of each bar is an important part of the DIRC enabling the capture of the Cherenkov light going forward into BaBar (the DIRC PMT readout is on the back side of the detector). Figure 29 shows the DIRC mirror reflectivity as a function of wavelength. The manufacturer’s data was found to be consistent with our data at three different laser wavelengths 266, 325, and 442 nm.

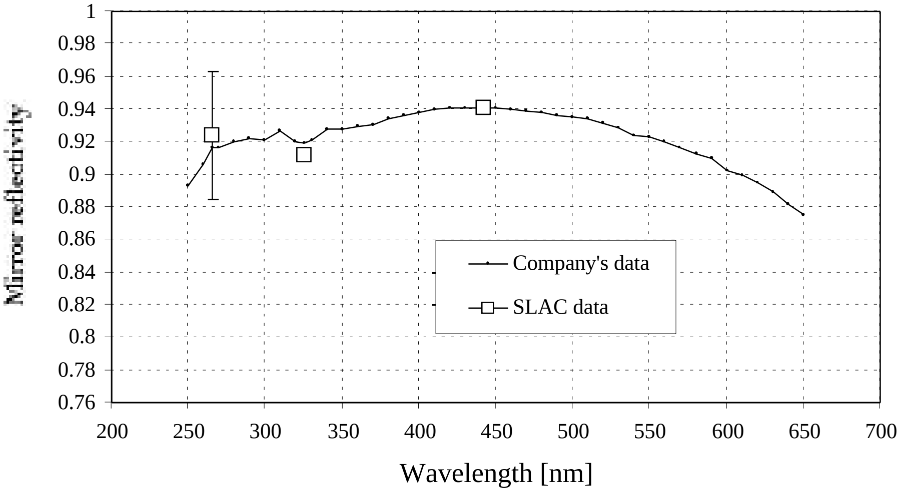

Figure 29. DIRC mirror reflectivity as a function of wavelength is shown. The data is measured with a laser, the mirror is in air, the laser beam is perpendicular to the mirror, and it is polarized vertically. The mirror manufacturer’s data are measured with the monochromator [11].

The fused silica bars have to be supported within the bar box. The idea is to choose a material that minimizes the reflection loss when a photon reflects from it. At the same time, the coupling between the fused silica bars and the aluminum bar box must prevent scratching of the fused silica surface given the differential thermal expansion. Figure 30 indicates that, for example Nylon creates very large reflection losses. This is true for all of the soft plastic materials tested such as Teflon or Rubber. The harder plastic materials, such as Kapton or Mylar, perform better. Metals, such as Aluminum, perform even better. Figure 30 indicates that the reflectivity of any material depends on the pressure with which the material is pressed against the fused silica bar. To quantify this better, we constructed a shim press, which was calibrated to express the force per area in psi units. Figure 31 shows the reflection losses with Aluminum shim foils as a function of the load. One can see that the loss is less than 1% for typical practical loads. For comparison, Fig. 32 shows that the uncoated Kapton or Mylar shims would be a worse choice.

There is an interesting physical explanation of these tests: a portion of the internally reflecting wave extends beyond the fused silica boundary and probes the medium on other side. The reflection can occur with a certain probability as a result. This effect gets larger as the laser wavelength decrease and is also sensitive to the proximity to the critical angle. This effect is used for commercial pollution studies, usually in the infrared wavelength region. In our case, as the force on the shim gets larger, this effect increases, resulting in the reflection coefficient decrease.

Based on these tests, DIRC has chosen Aluminum as the material for shims between the bars, and Nylon for the supporting buttons separating the bars and aluminum bar box.

---

[13] The DIRC mirrors were manufactured by United Lens Company, Inc., 259 Worcester Street, Southbridge, MA 01550-1325.

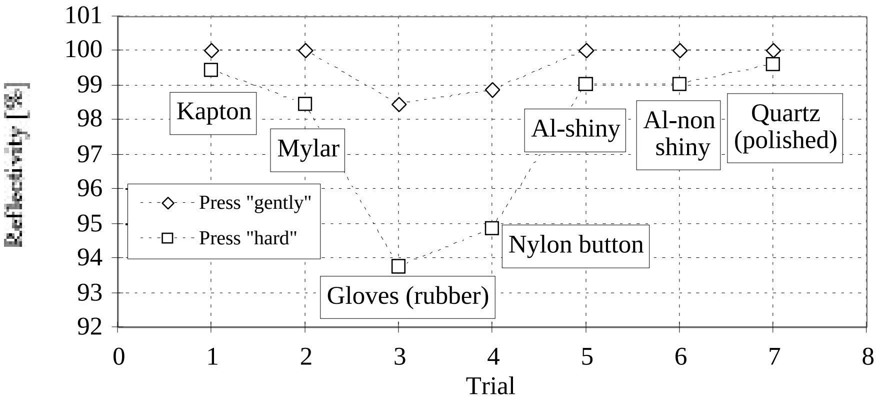

Figure 30. The single bounce reflectivity from various materials, which are attached to the bar at a place of reflection. This result motivated us to construct a press to quantify the results by knowing the loads on the shim [5].

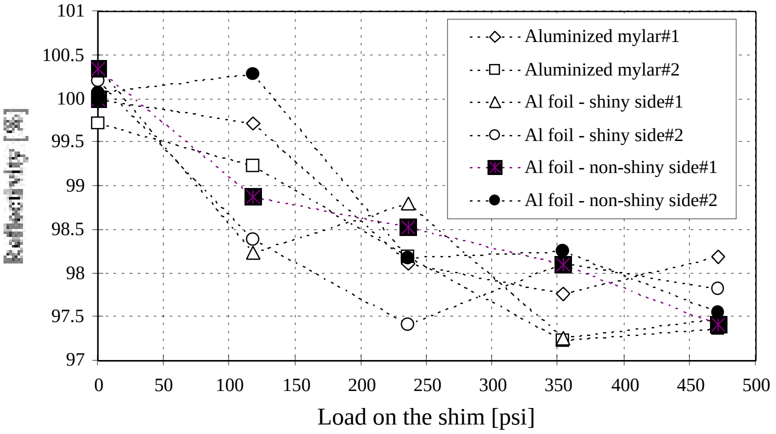

Figure 31. A single bounce reflectivity from the aluminum shims, which are attached to the bar at a point of reflection. We used the non-shiny aluminum shims to separate the bars in DIRC. The measurements were performed at 442 nm and incident angle of 21.5º [5].

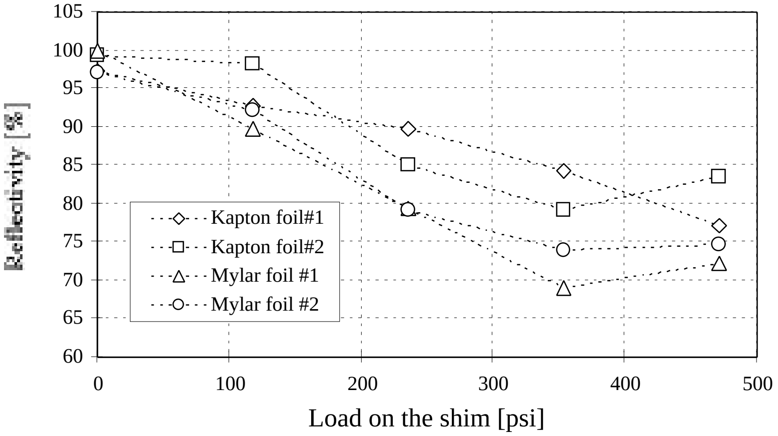

Figure 32. A single bounce reflectivity from uncoated Kapton or Mylar foils, which are attached to the bar at the point of reflection. The measurements were performed at 442 nm and incident angle of 21.5º [5].

7. DIRC FUSED SILICA BAR MECHANICAL QUALITY

The mechanical bar properties, such as the bar surface orthogonality or damaged edges would clearly influence the quality of the Cherenkov angle image or the number of photons detected. The primary goal of our setup was to validate the manufacturer's[14] bar measurements and provide independent measurements to double-check possible errors. To perform these QC checks at SLAC, we have built a digital microscope [8] and wrote several image-treating analysis programs based on the NIH Image software.[15] One of our codes was based on a manual operation, where an operator would follow an edge of the bar visually, clicking on several points along the edge to digitize its coordinates. Such points were then used in the fit to find a straight line. Using two straight lines one could then define the orthogonality of two surfaces of the bar.

Another algorithmic approach was to use all available pixels within a given view, and this is what we will describe in more detail. Each digitized picture consists of an array of 640 by 480 pixels, each of which has 8 bits of grayscale information. For each picture, the bar edges are found by stepping through each row and column of the pixel matrix and looking for the transition between black and white with a simple threshold algorithm looking at the gray scale information. A typical bar edge would consist of several hundred points, which were used to define the edges. A special line-fitting algorithm was needed to reject those points lying on "chips". We have achieved fitted resolution of about 1 micron. This method was then used to measure the fused silica bar's angles by making an image including two edges. The manufacturer used a micrometer-based fixture to measure bar angles, and this method was occasionally calibrated with the auto collimator (this method yielded a precision of approximately 50μrad). Comparing differences in side-to-end and face-to-end angle measurements using our method and the Boeing method, yielded a fitted error of less than 0.15mrad, which gave us a confidence that the two methods are consistent and can be used to reject bars that are out of tolerance. The face-to-side angle measurement comparison gave somewhat worse agreement of about 0.23mrads. We have accepted bars to be used in the DIRC using the following statistical procedure: we use all four face-to-side angles on both sides of the bar and calculate the rms of the eight values. The production tolerance was 0.4mrad for the rms of eight values, with a goal of 0.25mrad in each angle. Figure 33 shows a good agreement between rms measurements by Boeing Co. and SLAC, which gave use a confidence in company's data.

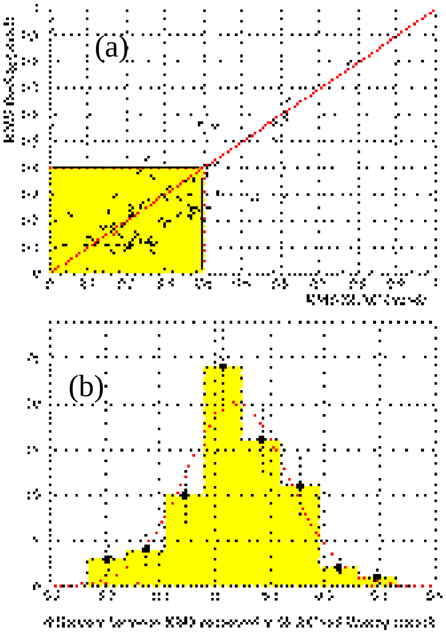

Figure 33. (a) Scatter plot shows the rms measurements made by Boeing and by SLAC. The rejected bars are outside of the shaded rectangle. (b) Difference between two measurements of the rms quantity defined in the text.

---

[14] Boeing Optical Fabrication, 2511 C Broadbend Parkway NE, Albuquerque, New Mexico 87107.

[15] NIH Image is a public domain image processing program.

Finally, the digital treatment of the entire image allowed also the quantitative analysis of the “chippy” edges. Figure 34 shows an example of a good and bad bar edge as seen by the microscope and the corresponding software. The measured total integrated damage per bar was less than 3x10^{-4} of the total area, of which the bar edges represented less than 20%.

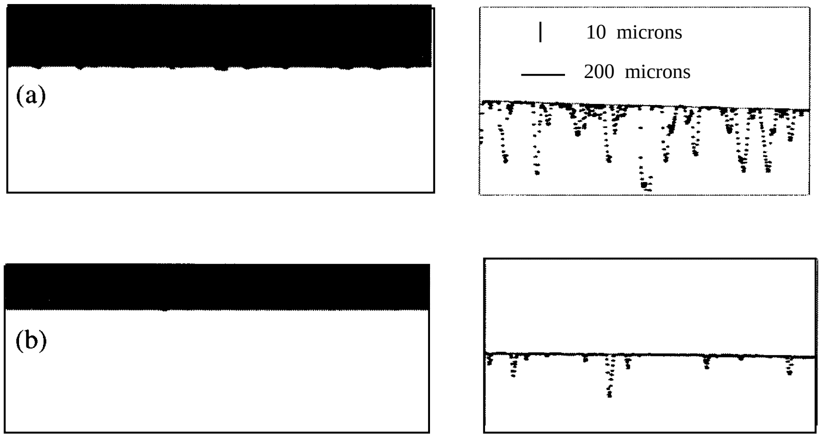

Figure 34. Example of (a) bad bar edge, as it appears on the Macintosh screen used for the microscope readout (left side), and the digitized version of the same edge by the off-line software analysis (right side), and (b) the same for the good bar edge, which was typical [8]. Note that even for badly damaged edges, the algorithm finds the “true” edge with good accuracy. The image has been greatly magnified in the y-direction.

CONCLUSIONS

1. This paper shows that natural fused quartz materials can suffer from serious radiation damage in the blue, and, particularly, in the UV regions after exposure to a radiation dose of 5-10 krad using a Co^{60} source. Although transmission recovery is possible using photo-bleaching and/or heating treatments, such "curing procedures" are not practical for BaBar. We also found that some natural fused quartz materials, most notably T-08, suffer from radio-luminescence at room temperature. All synthetic fused silica samples were found to be sufficiently radiation hard for BaBar. There are some small variations in the radiation damage rate among various materials, probably related to different levels of impurities.
2. All optical glue candidates tested so far are radiation hard at a level of 5-10 krads, which is the dose expected at BaBar. At the 70 krads level, there is a 1% degradation in transmission for the EPOTEK 301-2 epoxy, which was selected for gluing the bars.
3. The tests show that some synthetic fused silica materials, made in the form of ingots, show periodic optical inhomogenieties. This was an extremely important discovery, because in some instances this effect would make the DIRC inoperable.
4. We also present measurements of the wavelength dependency of, (a) the absolute value of the internal reflection coefficient, (b) the bar transmission, and (c) the mirror and supporting shim reflectivities.
5. All results presented in this paper provide supporting evidence of the importance of the extensive R&D conducted during DIRC development and construction. Furthermore, it is now apparent that without this program, the DIRC would have not worked well.

ACKNOWLEDGMENTS

We would like to thank H. Krueger for important contributions during his 1996 summer stay at SLAC. We also thank R. Reif, M. McCulloch, and M. Schneider for their excellent technical help.

REFERNCES

1. B. Ratcliff, SLAC-PUB-6047, January, 1993.
2. This parameterization of the fused silica refraction index comes from the Melles-Griot Company’s catalog,

which is taken from I. H. Malitson, Journal of the Optical Society of America, Vol. 55, No. 10, October 1965, pp. 1205-1209. The quoted accuracy of index is ±3x10^{-5}.

3. The refraction index data come from N.I. Koshkin, M.G. Shirkevich, Handbook of Elementary Physics, 1982.
4. The EPOTEK Company provided data of refraction index of EPOTEK 301-2 optical glue at 589.3 nm (a sodium D line) and few wavelengths in the range of 1000-5000nm.
5. J. Va'vra, "Quartz absolute internal reflection coefficient, water transmission, mirror reflectivity, mean wavelength response, mean refraction index, and their effect on the expected number of photoelectrons and N_o," BaBar DIRC Note #129, April 12, 2000; see also Nucl. Instr. & Meth., A453 (2000)262-278.
6. M. Convery, B. Ratcliff, J. Schwiening and J. Va'vra, "Measurement of Periodic Structure in Synthetic Quartz," BaBar DIRC Note #130, April, 2000.
7. K. Abe et al., Nucl. Instr. & Meth., A343 (1994) 74-86.
8. J. Cohen-Tanugi, M. Convery, M. McCulloch, R. Reif, J. Schwiening and J. Va'vra, "Development of a Digital Microscope for the DIRC Quartz bar Quality Control," BaBar DIRC Note #132, May, 2000.
9. S. Yellin, "Diffraction from an Oscillating Refractive index," BaBar DIRC Note #75, 1999.
10. H. Krueger, R. Reif, X. Sarazin, J. Schwiening and J. Va'vra, "The Optical Scanning System for the Quartz Bar Quality Control," BaBar DIRC Note #54, October 11, 1996.
11. J. Cohen-Tanugi, M. Convery, J. Schwiening and J. Va'vra, "The First DIRC Bar Box," BaBar DIRC Note #122, April 19, 1999.
12. H. Krueger, R. Reif, X. Sarazin, J. Schwiening and J. Va'vra, "Measuring the Optical Quality of Quartz Bars and the Coupling of RTV to the Window," BaBar DIRC Note #40, May 20, 1996.
13. H. Krueger, M. Schneider, R. Reif and J. Va'vra, Initial Measurements of Quartz Transmission, Internal Reflection Coefficient and the Radiation Damage," BaBar DIRC Note #18, January 5, 1996.
14. J. M. Elson, H. E. Bennett, and J. M. Bennett, Scattering from Optical Surfaces, Applied Optics and Optical Engineering, Vol. VII, Chapter 7, Academic Press, Inc., ISBN 0-12-408607-1979.
15. J. Cohen-Tanugi, M. Convery, J. Schwiening and J. Va'vra, "Study of the Internal Reflection Coefficient of DIRC bars as a Function of Quartz Surface Pollution", BaBar DIRC Note #131, April, 2000.
16. I. Adam et al., SLAC-PUB-7706, November, 1997.
17. R. Aleksan et al., Nucl. Instr. & Meth., A397 (1997) 261.
18. C.E. Barnes, IEEE Trans. Nucl.Sci., Vol. Ns-29, No.6, Dec. 1982, p. 1479.
19. X. Sarazin, M. Schneider, Schwiening, R. Reif and J. Va'vra, "Radiation Damage of Synthetic Quartz and Optical Glues," BaBar DIRC Note #39, October 15, 1996.
20. S.W.S. McKeever, "Thermo-luminescence of solids," Cambridge Solid State Science Series, Cambridge University press, p. 187, 1988 edition.